LIGO
Seismic Isolation Design
Study Report

April 28, 1994

1.0 Introduction

The intent of this briefing document is to summarize work in progress on the vibration isolation mount for the LIGO project as of 28 April 1995. Design of a prototype isolation mount, entitled Seismic Isolation Stack (SIS) was initiated in the latter part of February 1995. The primary objectives in developing a prototype SIS were to demonstrate:

- effective attenuation of all subseismic and cultural induced vibration over a bandwidth of 10 to 1000 Hz,
- a passive isolation stack concept employing metallic springs, viscoelastically damped to eliminate undesirable structure resonances,
- high stability through minimization of creep and thermal effects,
- and compatibility with a ultra-high vacuum environment.

To achieve these objectives the SIS must be a low frequency resonant structure that attenuates lateral and vertical modes of vibration at frequencies above 5 Hz. Although, the low frequency resonant requirement points to a massive stack structure, and objective of the prototype design was to minimize system mass where practical. As construction cost of the SIS is strongly influenced by the amount of material and the fabrication techniques, it was judged desirable to minimize stack mass and employ simple conventional fabrication methods wherever possible.

As conceived in February 1995, the major elements of the SIS prototype development program were to:

- conduct a materials study effort,
- select candidate materials for the spring structural and energy dissipation elements,
- analyze potential mechanical spring geometries, and method of SIS damping
- fabricate a prototype(s) spring element and test to establish frequency response characteristics,
- conceptually design the SIS and analyze it's isolation performance,
- fabricate and test one layer of the prototype isolation stack, and
- set-up interferometric based sensing equipment capable of making extremely precise measurements of structural mode shapes, response frequencies, and displacements.

The project as outlined has been in place nominally 9 weeks. During this period we have concentrated on the materials study and the definition of the spring geometry. Material study activities comprised both extracting from literature material property data, as well as initiation of material testing using TV Holography, an interferometric based measurement system. During the latter portion of the program effort, briefing documents were initiated in preparation for a project review in May 1995. At this juncture, a stop work order was received 18 April 1995 with an effective date of 3 May 1995. The reason for the stop work order was for a matter unrelated to the progress on the subject contract.

In compliance with the directive, we focused on completing the briefing document. Material testing was drastically reduced as a result of this directive, although several important results were obtained and this information is contained herein.

2.0 Discussion Of Summary Charts

The enclosed charts are in viewgraph format. They were being prepared for the purpose of briefing LIGO project personnel at California Institute of Technology on the status of the SIS prototype development. Clearly, the number of charts are too numerous for a single briefing. Selected charts would be extracted from this compilation for the actual presentation. The attached charts do reflect the scope of the study underway, and also provide insight to areas that would require more study. In this brief period we developed a growing understanding of the many design issues. The following is intended to give highlights of these issues.

Material Damping.- In our study we were interested in the internal damping of the structural materials (metals) that potentially would be used in the isolation stack and springs. Material damping is associated with internal friction mechanisms that can be quite complex for the strain amplitudes we anticipate for the LIGO SIS. The alternating stress induced in a structure excited at resonance conditions can be appreciable. The engineer's task is to maintain this stress state within acceptable bounds, through the appropriate choice of materials and damping techniques. However, if one is to achieve the attenuation objectives set forth for the LIGO SIS, the strain amplitudes must be restricted to levels many orders of magnitude below normal engineering standards. The LIGO SIS must be a stable, precision system where the regime of strain amplitudes lie in the nanostrain to microstrain domain. Much of the available material data is in the 1000 microstrain and above regime.

A cursory review of available material damping data is summarized in chart WM-LIGO-49. This chart is contained in the section on springs (unfortunately the charts are not sequential). Los Alamos National Laboratory performed TV Holographic measurements on two material specimens, Aluminum 5052, and Beryllium Copper in the 0.1 to 10 microstrain regime, in support of our materials investigation. More will be said about this test program later. The material chart summarizes potential spring material candidates. We listed key parameters of interest in the material selection process, elastic modulus, design stress, modulus of elastic resilience, and loss factor η. In the course of this briefing one would hope to point out that these materials exhibit anelastic behavior, and their representation in analytical models would resemble the treatment for viscoelastic materials where the loss factor exhibits frequency dependence. One will find through closer inspection that at very low strain amplitudes the metal's loss factor will exhibit dependence on strain amplitude as well.

Constrained Layer Damping.- We also initiated the task of identifying the viscoelastic damping material candidates for the constrained layer damping concept proposed for the

LIGO SIS. The loss factor η and real elastic modulus for two candidates are shown in charts WM_LIGO-38 and 41. These charts were extracted from a viscoelastic material (VEM) data base. The VEM database allows a designer to search for a material based on the properties of temperature, frequency, modulus, and loss factor. This is accomplished using the mathematical relationships from characterization. Since it is impossible to test a viscoelastic material at every combination of temperature and frequency for modulus and loss factor, the material is tested at discrete temperatures and frequencies and then two mathematical relationships are developed that characterize the material at all other combinations of temperature and frequency. This process, known as characterization, allows the four dynamic material properties of temperature, frequency, real modulus, and loss factor to be displayed in a meaningful manner on a single plot, known as the constant-frequency nomogram, or international plot. The use of the international plot to read interpolated values of real modulus and loss factor is demonstrated in chart WM-LIGO-39. To obtain real modulus and loss factor values corresponding to 100 Hz and 20°C, one reads the 100 Hz frequency on the right-hand scale and proceeds horizontally to the 20°C temperature line. Then proceed vertically to intersect the curves along a line of reduced frequency. Finally, proceed horizontally from these intersections to the left-hand scale to read the value for the real modulus and the loss factor.

Most VEMs can be assumed to be thermorheologically simple, which can be characterized using a frequency-temperature equivalence. A temperature shift curve, α_T, which is a function of temperature only, is constructed for each particular set of complex modulus data. The real part, G_R the imaginary part, G_I, and the material loss factor, $\eta=G_I/G_R$, of the complex modulus data are plotted as a function of the reduced frequency, f_R, where f_R is the product of the experimental frequency, f_{exp}, and α_T ($f_R = f_{exp}\alpha_T$). Historically, the temperature shift function for a particular damping material has been defined empirically by the experimental complex modulus data. The value of α_T at each experimental temperature is selected such that it simultaneously shifts horizontally the three complex modulus data points G_R, G_I, and η to define curves and minimize scatter. With the use of computers, it is convenient to fit the empirical temperature shift function with a suitable analytical function of parametric nature.

Additional work is needed in this selection task, coupled with analyses to establish the requisite visocelastic material modulus for the constrained layer.

Computational Methods.- Modeling of a structure comprised of metal springs, viscoelastically damped, will require special treatment. We anticipated that care would be required in this area. We did not, however, anticipate that the finite element code we used extensively in many of our stable structure design studies is not adequate for the LIGO task, whether viscoelastic materials are used or not. Using a modal analysis technique to predict the response of base excited structures results in an over-damped performance prediction. Transmissibility charts of simple spring-mass models are shown in WM-LIGO-34 and 35. In these models, the base motion was input as a harmonic excitation of unit amplitude. At frequencies above the unity gain frequency, one expects an ideal roll-off of

$1/f^{2n}$ where n corresponds to the model degrees of freedom. Clearly, this does not occur, and the problem is caused by the damping being assumed to be proportional to the masses' velocity of motion. Solution techniques involving complex representation of the damping that overcome this problem are available, the MSC/Nastran Code being one example. We recommend utilizing this code on models of the structural materials, as well as the viscoelastic materials.

Spring Sizing.- Calculations were made for a structural spring element that is based on a conical shell concept. The results of these preliminary calculations are contained in the section on Spring Concept Study. The principal objective of these calculations was to establish what range of spring rates could be achieved by simple geometry changes. A range in spring rates from roughly 10 kg/cm to 800 kg/cm was obtained through varying material thickness, shell inside and outside diameters, and splitting the conical shell. The split conical shell provides a cantilever flexure arrangement that also affords an opportunity to control the spring bending stiffness. In conjunction with this task, a proportioning of the spring column rate, i.e., between the plates was initiated. One may realize that the spring, or springs, supporting the upper plate would be less stiff than the spring, or springs, that supported the bottom plate in the overall stack. The spring static design stress needs to be evaluated, particularly for the bottom spring, or springs that must bear the entire weight. Local yielding of the material from bearing the static weight was to be avoided.

Material Testing.- Various approaches for performing precision material measurements and modal testing were considered during this initial program phase. We visited several companies that offered differing capabilities in this regard. From past experience on other stable structure projects, we recognized that expeditiously setting up a precision measuring capability would be difficult. We were also concerned with establishing what truly were the technical issues in making these particular measurements, as they differed somewhat from the previous experience base. A technical assistance partnership was established with Los Alamos National Laboratory to explore these matters with their TV Holography system. The detailed results of this investigation is contained in a latter section. The outcome of this effort pointed to the difficulties one would encounter in making loss factor determination in an extremely low strain amplitude regime.

We made a decision to test specimens utilizing existing test facilities and interferometric based test apparatus. This permitted an early evaluation of the issues involved without committing the resources assigned in the SIS project for this effort. The results of these tests are contained in the section following the briefing documents. Normally the next step one would take in following through on the planned LIGO SIS experimental test activity would be to carefully digest these results, and to implement modified test methods to overcome the test issues uncovered.

For the preliminary tests, we secured beryllium copper and viscoelastic tape specimens from Berlyco and 3M respectively. Although, time did not permit a thorough study of constrained layer damping we did measure a loss factor of 0.2 on our first sandwich

attempt. This is a 100 fold increase in damping over the parent material, at very low strain amplitudes. Our initial investigation was intended to explore loss factor for the parent material, at two different hardnesses, and loss factor for two constrained layer sandwiches. The layered sandwiched was one inch wide. The test matrix involved test combinations for two facing thicknesses, .635 and 1.27 mm, and two viscoelastic tape thicknesses, 0.127 and 0.254 mm, respectively.

3.0 Summary

The technical challenges in constructing a passive isolation stack to the LIGO specifications are significant. In a very short time we had began to explore the issues we had identified at the onset, and felt that we moving in the direction to find appropriate solutions. The experience gained in this brief period will provide valuable insight to anyone continuing with this effort. The results gleaned to date are not entirely conclusive, however, the information obtained does not indicate the existence of any "show-stoppers" that would prevent the realization of the technical goals.

4.0 Future Work

Preparing a detailed outline of future work would appear a bit contradictory in view of the present stop work order. It is judged that a brief listing of proposed activities is in order in spite of this obvious conflict. If work were to be resumed we would recommend one focus on the following tasks.

- **Stack Spring Rate.-** Complete the model of the isolation stack. The model was being used to solve for the spring rate distribution at each layer. As added step, set-up the model on the PC-version of MSC NASTRAN and use this structural code to obtain the proper transmissibility representation for the high frequency regime.
- **Spring Configuration Study.-** Continue the process of evaluating structural aspects of the conical spring concept. Provide the basis for selecting a geometry that simultaneously provide the desired vertical and lateral isolation frequencies.
- **Viscoelastic Material Selection.-** Review the current selection of candidate viscoelastic choices. Configure the constrained layer approach to achieved the desired damp response of the conical spring. Identify fabrication issues and work out details with material suppliers.
- **Material And Spring Module Test Program.-** Develop an approach to solve the test technique issues identified in the initial material tests. Seek a coordinated test program approach that utilizes outside vendor test facilities in a complementary way to any experimental tests proposed to be conducted using LIGO SIS resources, that require major acquisitions.

Some thought must be given to restructuring the basic program approach for the isolation stack development as a result of the stop work order. The momentum gained during the

short period of the program has been lost. Resumption of the tasks outlined for the SIS need to be re-baselined.

Program Objectives-Key Issues

Establish Technical Approach For Seismic Isolation Stack (SIS) That Satisfies Following Requirements:

Effective Subseismic Attenuation Over Band Width
10 Hz<f<1000 Hz

Reduction in Weight of Optical Table and SIS Over Existing Design

Materials Compatible With High Vacuum Environment

Minimization of Creep, and Thermal Effects

Kinematic Mounting of Optical Table

A Compact, Passive Isolation Mount Concept

Primary SIS Program Elements

Materials Selection For Structural and Energy Dissipation Members

Configuration Studies to Identify Approach For Metallic Springs With Enhanced Internal Damping Characteristics

Prototype Spring Fabrication and Testing To Establish Frequency Response Characteristics

One Layer of the Full-Scale LIGO Seismic Isolation Stack Tested For Frequency Response Characteristics

Material Activities-Current Areas of Emphasis

- Identify Candidate Spring-Like Materials and Materials for Damping Structural Modes of Vibration
  - Obtain Available Material Properties Relevant to Design In Areas of Strength, Elastic Characteristics, and Damping
  - Experimentally Establish Material Damping Properties To Supplement Design Information Based On Available Literature
  - Select Candidate Viscoelastic Materials for Enhancing Structural Damping
- Quantify Structural Damping Offered By Constrained Layer Damping Concepts
- Review Modal Damping Simulation in FE Codes for Suitability In Predicting The SIS Performance

MATERIALS STUDY

Considerations

- Candidate Spring Material
- Viscoelastic Damping Of Structural Elements

Preliminary Materials Test Results

MATERIAL DAMPING

Modal Analysis Of Multidegree Systems- Finite Element Analysis Of Linear Systems

- Normal Modes Of Vibration Are Orthogonal For The Viscous Damping Representation Assumed (Diagonal Damping Matrix)
- Solution Reduces To Solving Linear Set Of Uncoupled Single Degree Of Freedom Equations Where:
  - One-Degree of Freedom System Has Same Kinetic Energy, Internal Energy, and Work Done By All External forces As For The Complete System Vibrating In The Normal Mode

Very Powerful Technique And In General Satisfies Most Engineering Problems

We Have A Linear System, But Unfortunately We Can't Use This Method To Accurately Predict The SIS Transmissibility

Single Degree Of Freedom Model Based On 2% Modal Damping Base Excitation

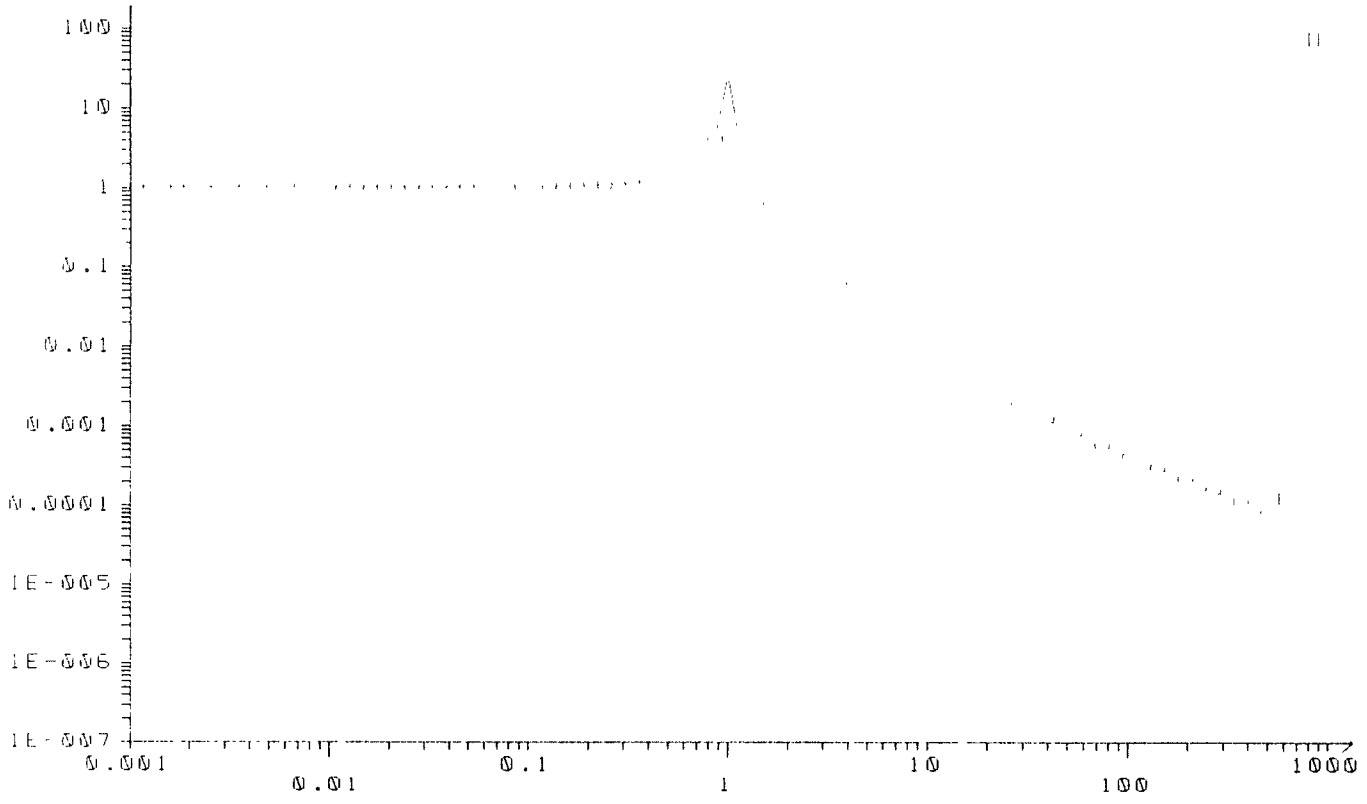

Modal Damping (Viscous Damping)
Over Damps At Frequencies Beyond Unity
Gain Frequency Point

Four Layer Isolation Stack
2% Modal Damping
Base Excitation

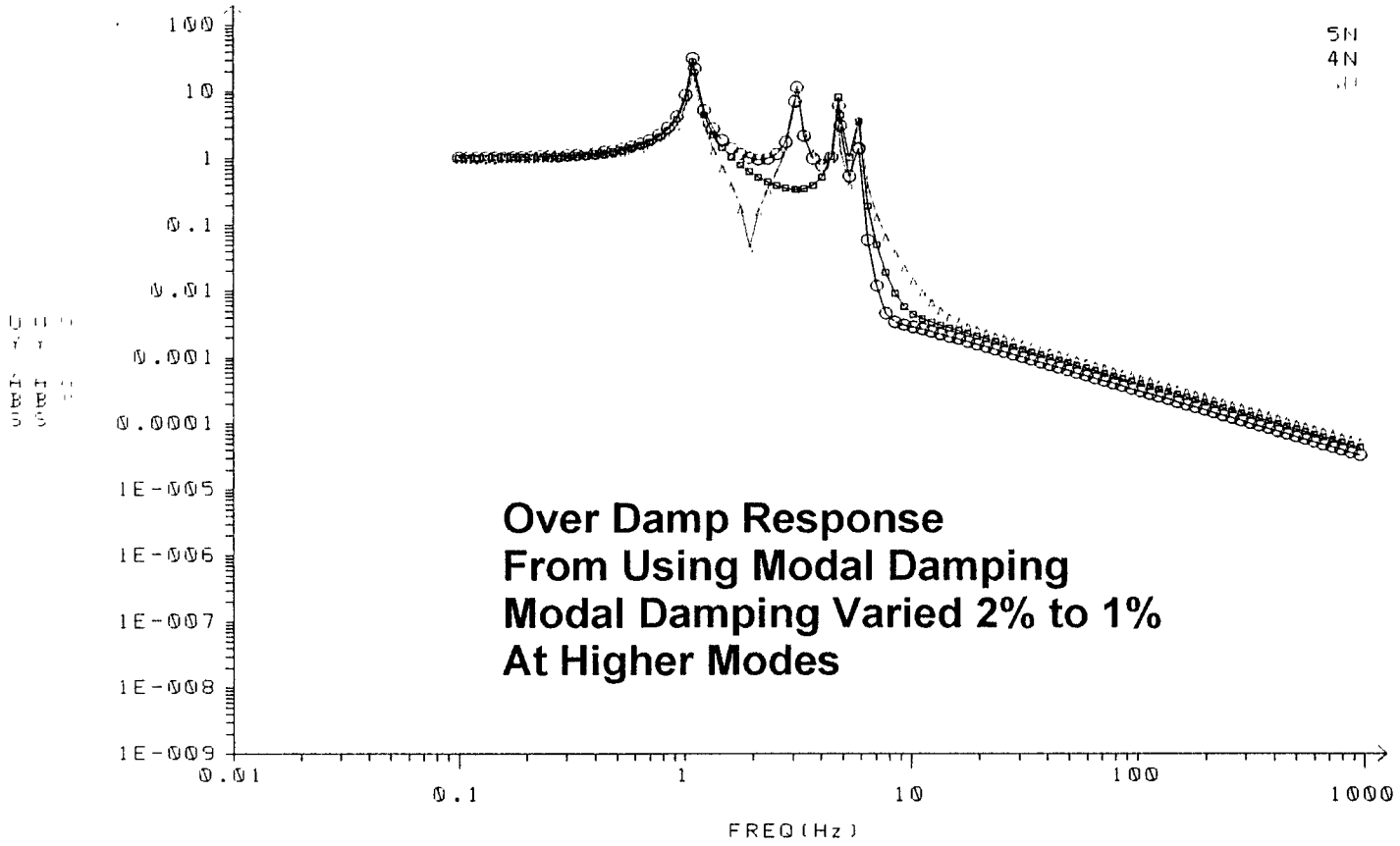

Over Damp Response
From Using Modal Damping
Modal Damping Varied 2% to 1%
At Higher Modes

4 Plates 454 kg's ea.
4 Springs With Rate
Of 178.6 kg/cm ea.

MATERIAL DAMPING

Finite Element Analysis Of Linear Systems - Support Motion

Material Damping Representation Must Use Complex Notation

> Provides Proper Representation Of Real And Imaginary Components Of Viscoelastic Damping Materials, Including Frequency Dependence

Finding Effective Modal Damping Value For Each Mode For The Viscoelastic Damped Structure And Thereafter Using Modal Damping Will Lead To Same Problem Of Over Damping

MATERIAL DAMPING

Inelastic Behavior of Materials, Composites, and Structural Assemblies At Very Low Strains Is Domain of Interest

In General There Are Four Possible Combinations Of Damping

- Rate-Dependent, Recoverable Behavior
- Rate-Dependent, Non-Recoverable Behavior
- Rate-Independent, Recoverable Behavior
- Rate-Independent, Non-Recoverable Behavior

Third Option Is not Considered Possible

- Rate Independence With Time Implies No Recovery With Time

We Will Be Dealing With The First And Second Cases

MATERIAL DAMPING

Rate-Dependent, Recoverable Strain - Anelasticity

Linearity, Doubling of Stress Doubles The Strain At Any Specified Time

Uniqueness Of Stress- Strain Curve, For Every Value of Stress Material will Achieve A Unique Value of Strain Given Sufficient Time

Rate-Dependent, Non Recoverable Strain -Viscoelasticity

Viscoelastic Strain May Have Recoverable And Non-Recoverable Components

In Sense Anelastic Behavior Is Special Case Of Viscoelasticity

MATERIAL DAMPING

Rate-Dependent, Recoverable Strain - Anelasticity In Metals

Hysteretic Damping - Inelastic Behavior Leads To An Elliptical Stress Strain Curve For A Linear Material

Internal Friction - Generally Found To be Independent of Strain Amplitude, However:

Damping Is Generally Found To Be Frequency And Temperature Dependent

We Are Interested In Intrinsic Material Damping Characteristics As Input To The Finite Element Models

Obtaining These Results Experimentally Is Dificult As Will Be Presented Shortly

MATERIAL DAMPING

Viscoelastic Linear Damping Materials

Variety Of Mechanisms In Real Materials Generally Lead To Similar Damping And Hysteretic Loop Phenomena

Under Sinusoidal Loading Hysteretic Loops Are Elliptical In Shape And Increase In Area With Square Of Strain Amplitude (Or Stress)

(Quadratic Damping Law)

Most Viscoelastic Materials At Low to Intermediate Stress, And Metals At Very Low Stress Display Linear Damping

Dissipation Force That Is 90° Out Of Phase With The Elastic Force

As A Matter of Introduction Let's Consider The Following

MATERIAL DAMPING

Damping Expression - Linear Damping

$D=J\sigma^n$ Where J And n Are Material Constants

For Low Strain Amplitudes We Find

n=2 - Quadratic Law
Hysteretic Loop Is Elliptical In Form

Relative Damping Expression, Ratio of Damping Energy To Strain Energy

$\eta=J\sigma^2/(2\pi U)$, Since $U=\sigma^2/2E$, $\eta=JE/\pi$, Independent of Stress

Loss Coefficient η Generally Considered Independent
Of Strain Amplitude, But In General Loss Factor Is Frequency
Dependent (As Will Be Shown Shortly)

MATERIAL DAMPING

Damping Expression - Linear Damping

$D=J\sigma^n$ Where J And n Are Material Constants

For Low Strain Amplitudes We Find

n=2 - Quadratic Law
Hysteretic Loop Is Elliptical In Form

Relative Damping Expression, Ratio of Damping Energy To Strain Energy

$\eta=J\sigma^2/(2\pi U)$, Since $U=\sigma^2/2E$, $\eta=JE/\pi$, Independent of Stress

Loss Coefficient η Independent Of Strain Amplitude, But Not Necessarily Independent Of Frequency As Will Be Shown Shortly

Hypothetical Stress-Strain Loops

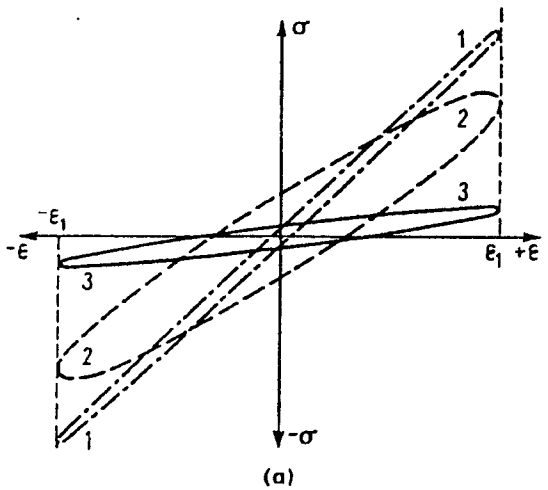

(a)

Cases

1 High Frequency or Low Temperature

2 Optimum Combination to Cause Relaxation Peak

3 Low Frequency or High Temeprature

Grain Boundary Peaks in Al

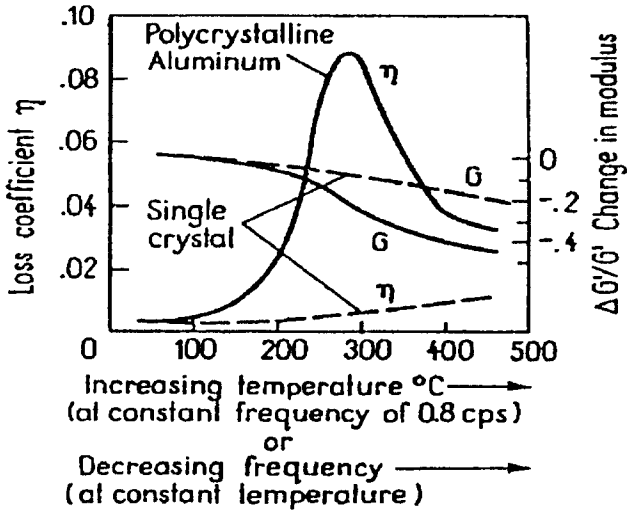

Three Classes of Linear Damping
Their Frequency Dependence and Symbolic Representation

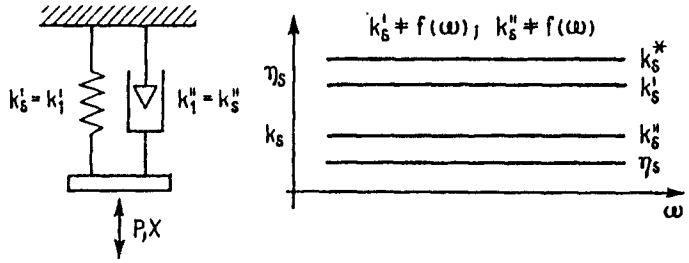

Rate-Independent

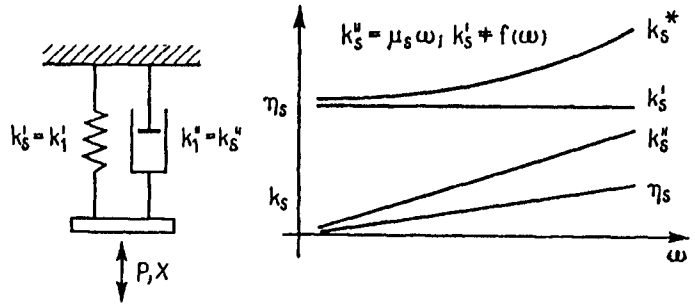

Linear Dashpot

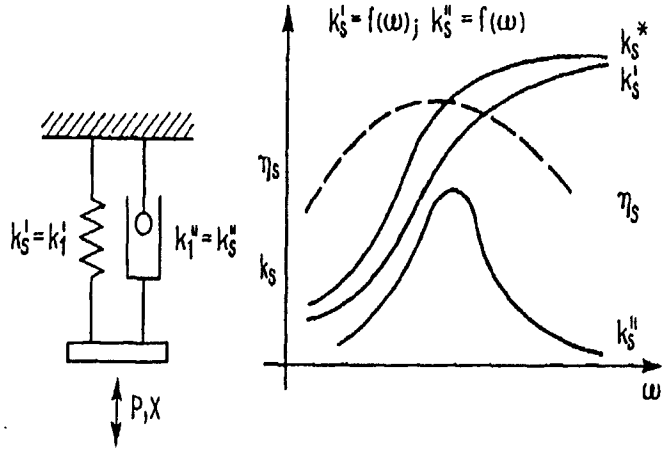

General Linear Damping

Where:

k'_s-elastic spring constant

k''_s-loss constant of spring

k^*_s-complex spring constant

Viscoelasticity as a Basis for Complex Notation (Voigt model)

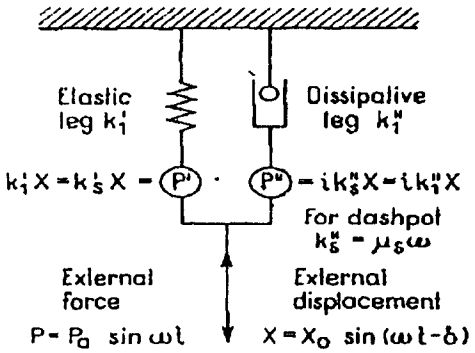

Parallel Bi-Parameter Model

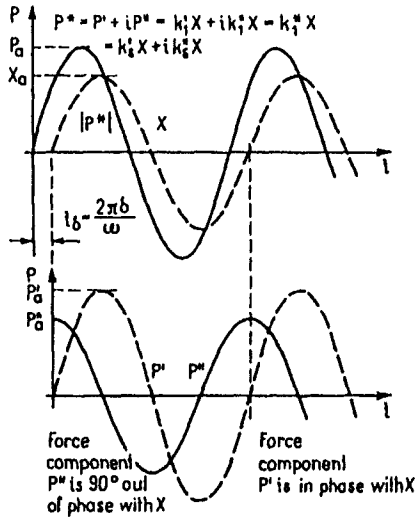

In-Phase and Out of Phase Force Components

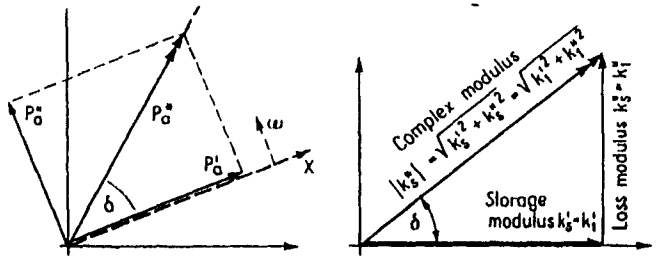

Vector Diagrams for Forces and Complex Modulus

MATERIAL DAMPING

Elastic System Definitions- For Voigt Model, Massless System

k'_1 , k''_1 , and k^* Are Properties Of The Component Parts

k'_s , k''_s , and k^*_s Are Properties Of The Entire Specimen Or Model

For Voigt Model the Corresponding Elastic Moduli Are Equal

$k'_s = P'_a / X_a$, Storage Modulus of System (In-Phase or Real Component Of the Spring Constant. For Materials The Equivalent Storage Modulus is E')

$k''_s = P''_a / X_a$, Loss Modulus Of The System (Out-Of-Phase Or Imaginary Component Of Spring Constant. For Materials The Equivalent Is E'' or G'')

Also $D_s = \pi k''_s X^2_a$

Loss Coefficient For Linear (And Non-Linear) Materials

$\eta_S = D_S/2\pi U_S$ Where D_S and U_S Are The Specimen Damping and Strain Energy Respectively

$\eta_S = \pi k''_S X^2_a / 2\pi (1/2 k'_S X^2_a)$ Since $U_S = 1/2 k'_S X^2_a$

$\eta_S = k''_S/k'_S = \text{Tan}\ \delta$ δ=Phase Angle

Loss Coefficient Is The Ratio Of Loss Modulus To The Real Storage Modulus, And Is A Measure Of The Phase Shift Between The Loss And Storage Moduli

Since For Our Simple Model The Elastic Spring Constant k'_S Can Be Conveniently Taken To Be Equal to AE'_S/L We Have In Effect:

$E'_S = (L/A)k'_S$ Simple Inversion Of The Expression For A Tension Spring Member

Real Modulus And Loss Factor
Viscoelastic Tape 3M Y - 4205

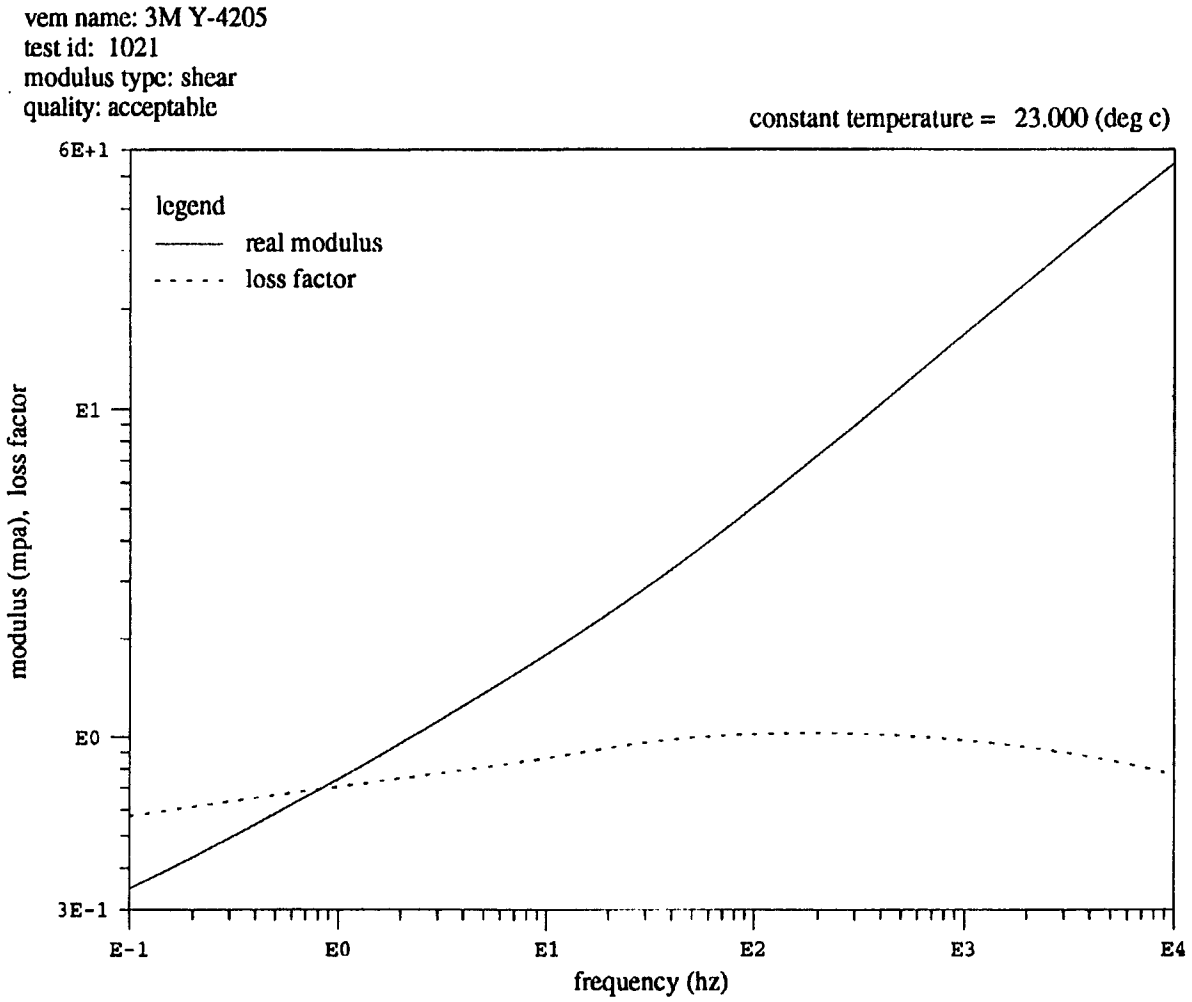

Real Modulus And Loss Factor
Viscoelastic Tape 3M Y - 9469

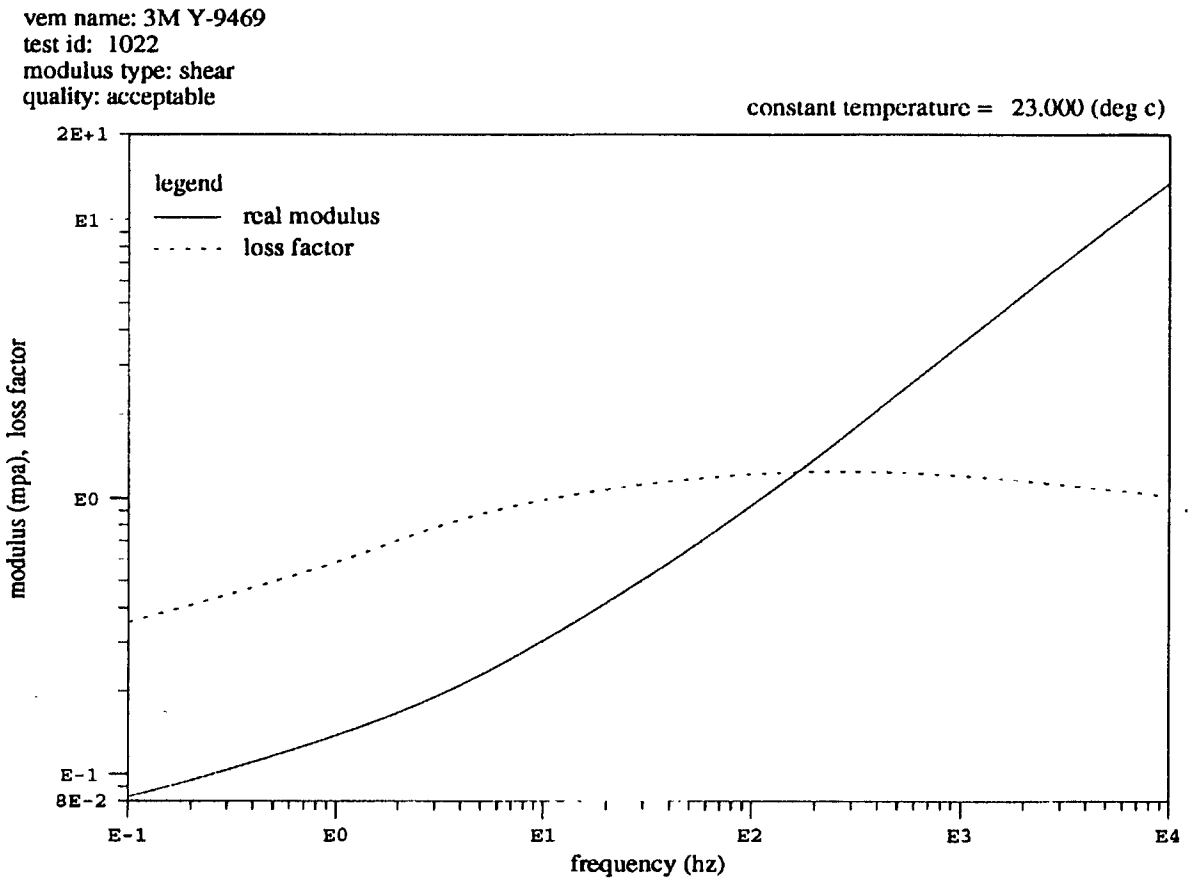

Reduced Frequency Plot
Real Modulus And Loss Factor
Viscoelastic Tape 3M Y - 9469

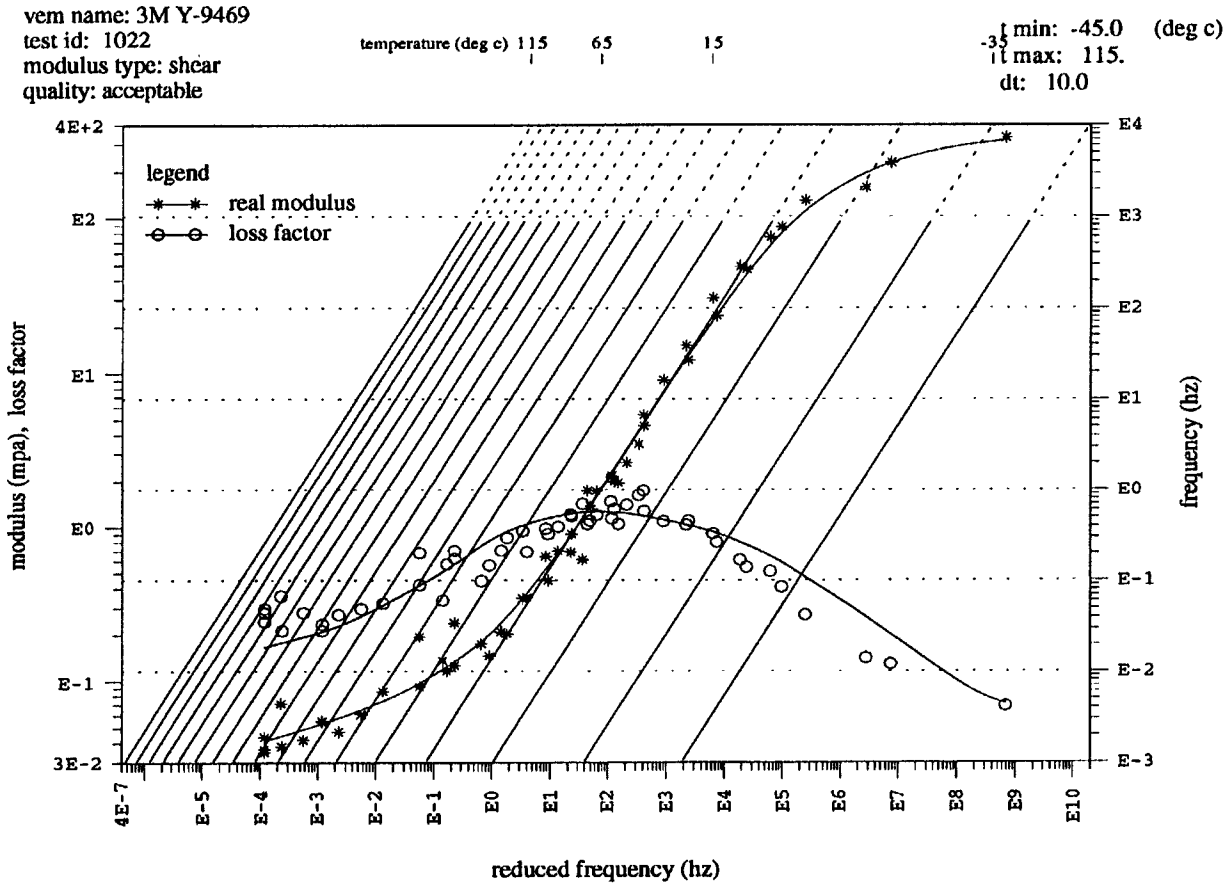

Effect of Temperature and Frequency On Storage Modulus, Loss Modulus, and Loss Coefficient of a Typical Polymer

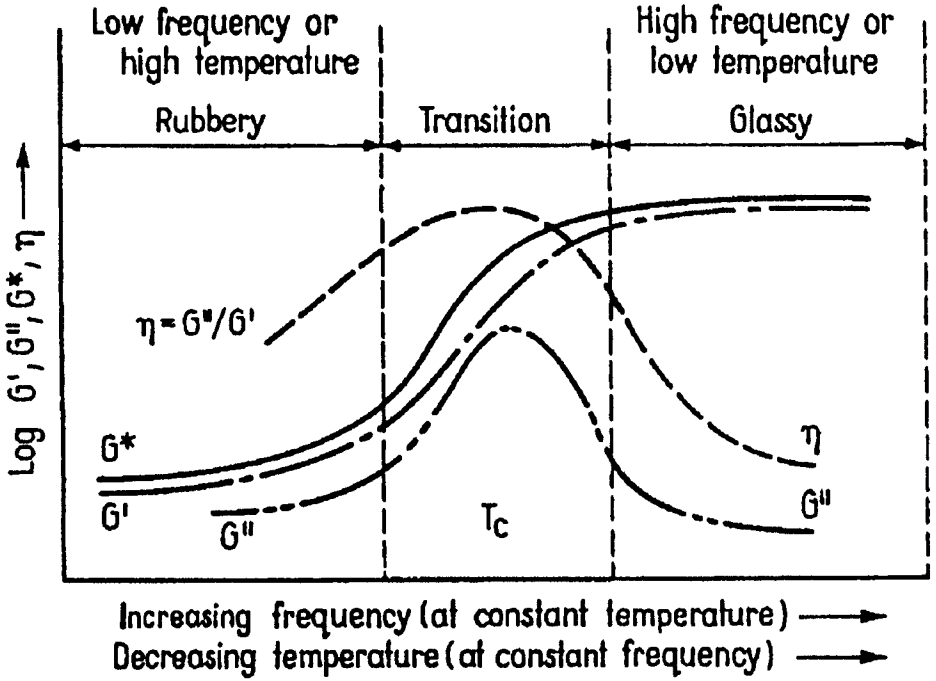

Storage Modulus of Elasticity E' versus E" and Loss Coefficient η_e for Various Materials

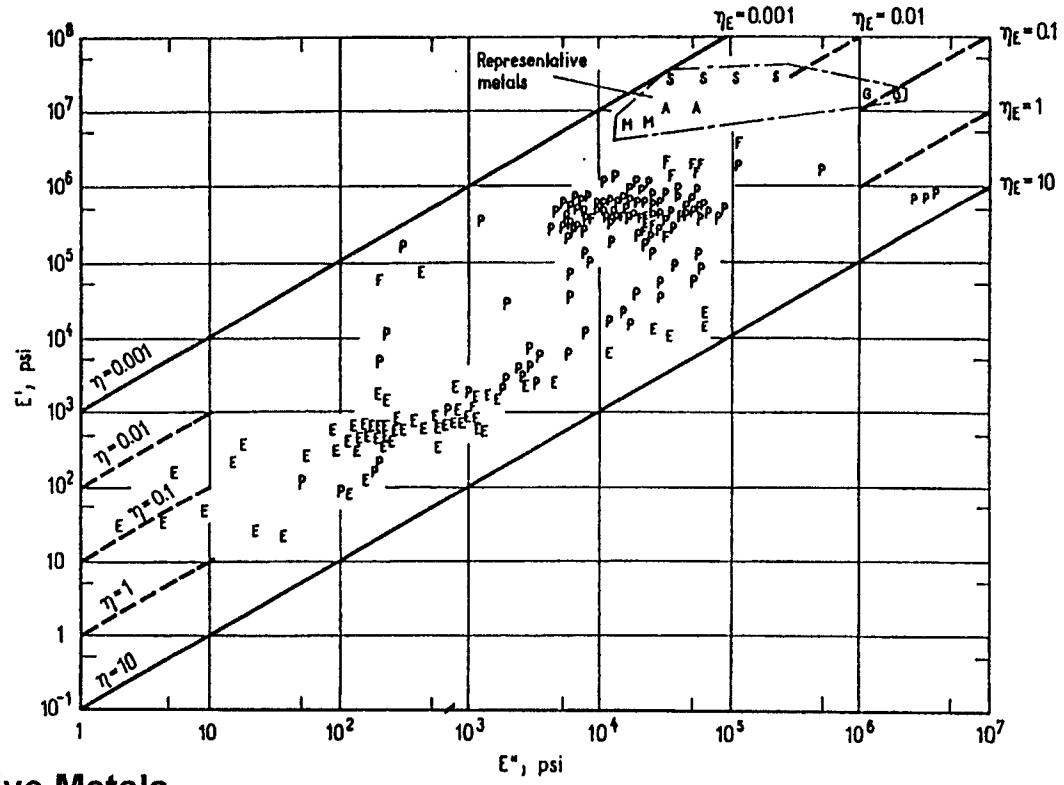

Representative Metals

- S=Steels
- C=Grey Iron
- A=Aluminun
- M=Magnesium Alloys

- P=Poylmers
- E=Elastomers
- F=Fibers

Storage Modulus of Rigidity G' versus Loss Modulus G" and Loss Coefficient η_e for Various Materials

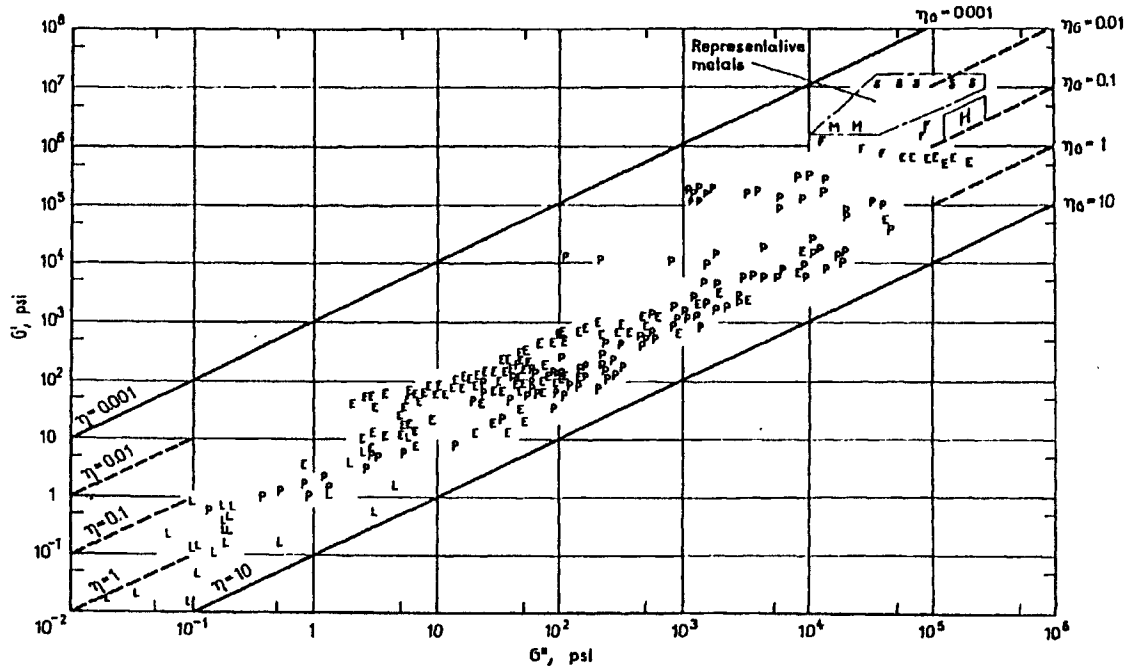

Representative Metals

S=Steels
M=Magnesium Alloys
H=High Damping Mn-Co and Magnetoelastic Alloys

P=Polymeric Materials
E=Elastomers
F=Fibers
L=Liquids

Presentation Of Introductory (Albeit Bit Simplified) Material Property Data For Low Strain Structural Response Domain Of Interest To LIGO Is Intended To Show:

- Material Loss Factors For Metals And Viscoelastic Materials Were Independent Of Strain Amplitude But Dependent Upon Frequency And Temperature
- Structural Modeling Of Material Damping And Structural Loss Factors Must Utilize Complex Notation To Allow Proper Representation Of Phase Relationship Of Damping And Structural Terms
- Conventional Modal Analysis Of Linear Systems Will Not Satisfactorily Model The LIGO SIS

Loss Factor Dependence On Strain Amplitude For Anelastic Materials Will Be Addressed Later With The Spring Material Discussion

Next Steps

- Continue Identification Of Potential Viscoelastic Material Candidates
- Model Viscoelastic Constrained Layer Concept To Establish Structural Loss Factor As Function Of Frequency
  - Select A Viscoelastic Candidate (s) For The SIS Spring Concept
- Establish The Loss Factor For The Structural Spring Element

SPRING CONCEPT STUDY

Spring Geometry Considerations

Candidate Spring Material

Initial Sizing Calculations

Spring Considerations

Modulus of Elastic Resilience

Resilience Is A Property Of The Selected Spring Material

Elastic Resilience Is A Measure Of The Strain That Can Be Absorbed Or Released By The Spring Within The Elastic Range Of The Material

High Modulus of Elastic Resilience Will Lead to More Compact Springs

For Tension Elements, The Resilience Modulus Equals $\sigma^2/2E$, Where E Is Young's Modulus, And σ Is The Material Yield Strength

In Bending, The Modulus Of Elastic Resilience Is Not Only A Function Of

Material Properties σ, E, But Also,
Geometry Of The Spring Cross-Section, And
Manner of Loading

Spring Considerations

Modulus of Elastic Resilience- Bending, Cantilever Beam Example

Cross Section	Elastic Resilience
Solid Cylinder	$\sigma^2/40E$
Thick Walled Tube	$\sigma^2/40E(1+(R_i/R_o)^2)$
Thin-Walled Tube	$\sigma^2/20E$
Solid Square	$\sigma^2/30E$
Constant Strength Cantilever	$\sigma^2/6E$

Where σ=Material Yield Strength, And R_i And R_o Are The Tube Inside And Outside Radii.

Spring Considerations

Spring Volume Efficiency - Geometry and Material Dependent

Work Performed / Spring Material Volume, W/V

Related To Material Elastic Resilience Through Factor K

Where for K We Have :

Helicoil Spring K = 0.4

Cantilever Beam K = 0.15

$W/V = K(\sigma^2/2E)$, The Helicoil Spring Is The Most Efficient On A

Volume Basis, Followed By The Simple Cantilever Beam

Initial Design Study For SIS Suspension Focussed On Cantilevered Beam Geometry

Spring Considerations

Cantilever Spring Concept - Perceived Advantages

- Reasonably Compact Compared to Other Options
- Predictable Stiffness and Modal Frequencies
- Compatible With Incorporation Of Viscoelastic Damping
  - Damp Higher Structural Modes
- Ease of Fabricability
- Vacuum Isolation of Polymer Materials Used In Damping

Spring Material Data

We Tend To Focus On Three Parameters

Maximum Design Stress - Region Of Linear Behavior

Elastic Modulus - Sets Spring Stiffness Along With Geometry

Material Loss Factor η - Corresponding To Low Strain Amplitudes ($Q=1/\eta$)

Data For First Two Parameters Readily Available

Loss Factor Data Is Available But Largely Corresponds To Test Conditions Of Relatively High Alternating Stress (Strain) Levels

LANL Interferometric Based Loss Factor Measurements Made For BeCu And Aluminum At Low Strains

Difficulty Encountered In Obtaining Repeatable Results

Spring Material Properties

Material	Condition	Maximum Design Stress σ_{max}-MPa	Elastic Modulus GPa	Modulus of Elastic Resilience (Tension) MPa	Loss Factor η
A229-41 Spring Wire	Ht, and oil quenched	772	207	1.65	(.002 to .03)[a]
UNS-S31600 Stainless Wire	Drawn, cold worked	1103	193	3.15	(.002 to .015)[a]
AISI-8650 Cr-Ni-Moly	Ht, tempered	1551	207	5.82	(.011)[a]
ASTM-B194 BeCu	Ht, by aging @ 600 °C	1172	128	5.4	.0026[b]
Reference Materials-Not Proposed For Springs					
ASTM-B48 O_2-Free Cu	35% Hard	331	117	0.47	(.003 to .04)[a]
5052-H32 Aluminum	Strain Hardened	215	70	0.33	.0022[b]

[a]Torsional tests @ relatively high strains [b]LANL measurements, 0.1 to 10 microstrain

Material Cantilever Test Set-Up
Piezo-Electric Driver

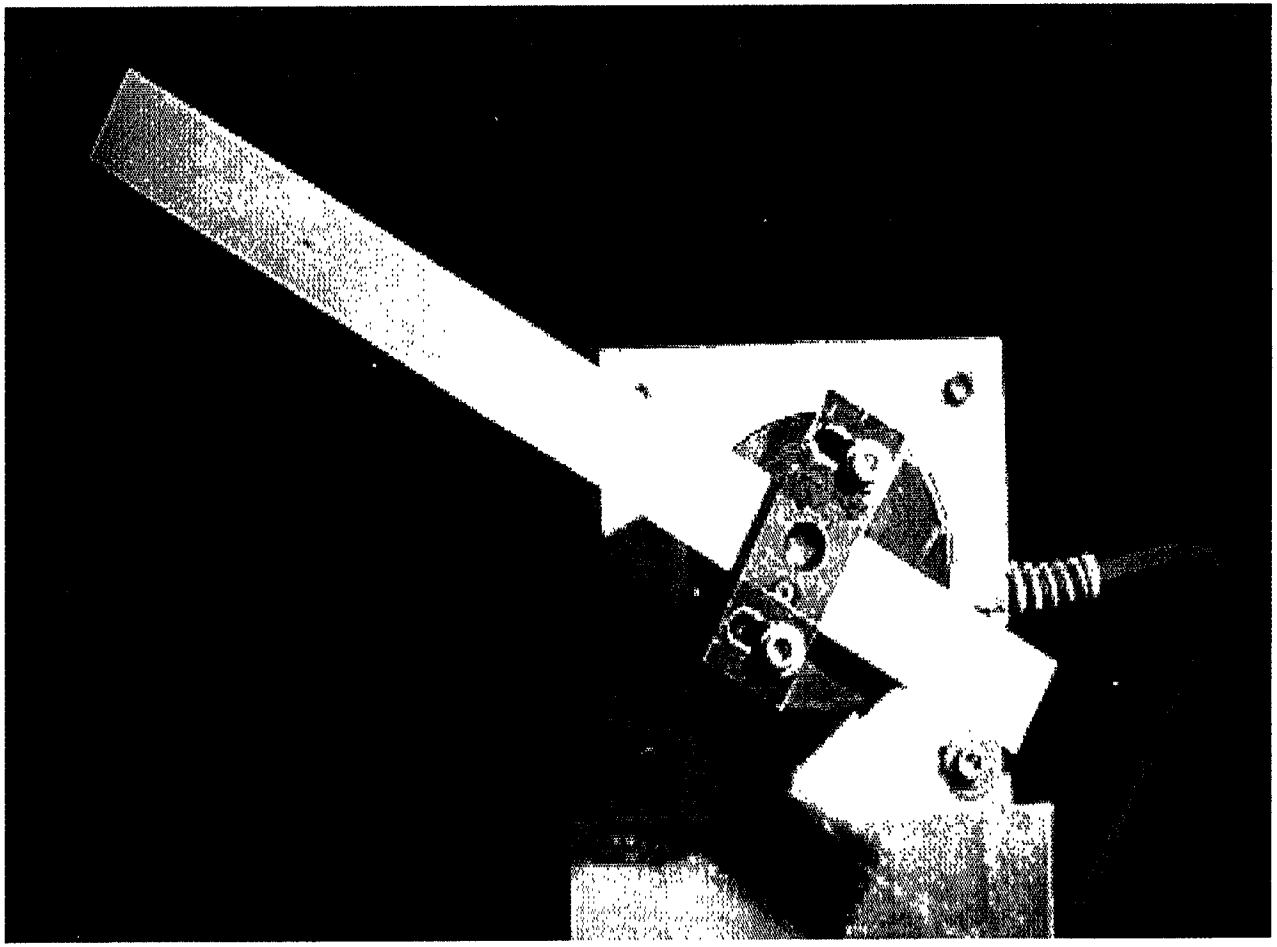

Test Arrangement For TV Holographic Measurements

SEISMIC ISOLATION STACK

TV Holographic Measurement Of Aluminum Specimen

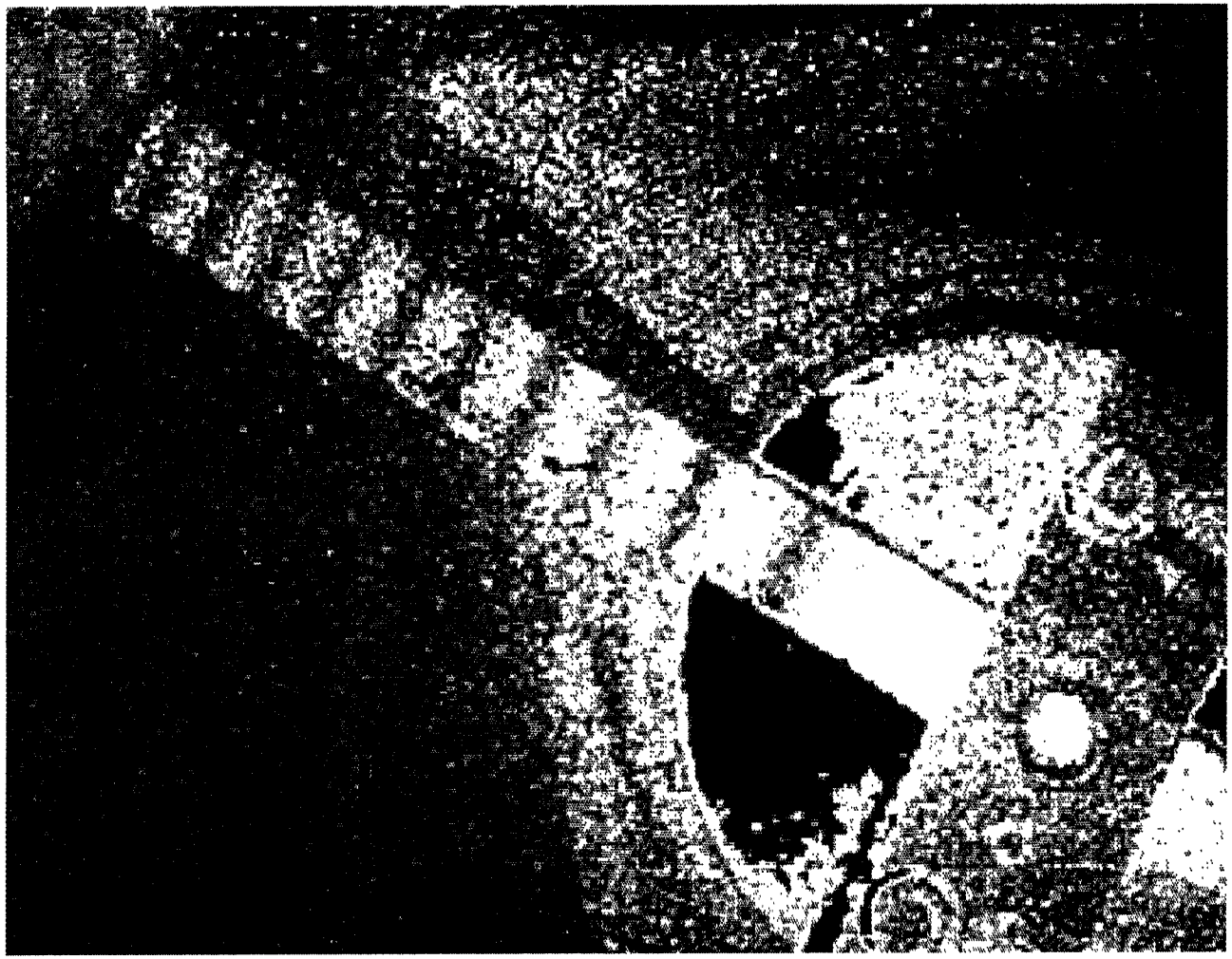

75.12 Hz

Loss Factor

η=.0025

Strain Regime

0.4 microstrain

Metals

Loss Factor - Nanostrain Levels To 1000 Microstrain
Ref. "Characterization Of Damping Materials And Structures
Nanostrain Levels To Thousand Microstrain By J. M. Ting, et al

Extremely Sensitive Measurements With Aluminum Show An Increase In Damping With Strain Amplitude (Range 1-1000 Microstrain)

@ 58.1 Hz Loss Factor Increased From .0018 To .008

As Expected, Frequency Dependence Of Loss Factor Was Also Reported

Loss Factor For Metals Is Associated Many Different Physical Mechanisms

Point Defect Relaxations
Grain Boundary Viscosity
Macro Thermoelasticity
Micro Thermoelasticity

To Name A Few - Mother Nature Hasn't Been Kind In This Regard

Metals

FEA Studies Of SIS Response

Internal Friction Loss Factors For Metals- No External Damping

- Selected Loss Factor Must Be Chosen For Appropriate Strain Amplitude And Resonant Frequency

Constrained Layer Damping- Loss Factor For Structural Element

- Analysis And Tests Required To Characterize Concept

Measurements Of BeCu And Al Constrained Layer Sandwich For Low Strain Amplitudes - By LANL

- Structural Loss Factor Two Orders Of Magnitude Higher

- Additional Tests Required to Confirm No Strain Amplitude Dependence And To Establish Frequency Dependence

CONICAL SPRING CONCEPTS

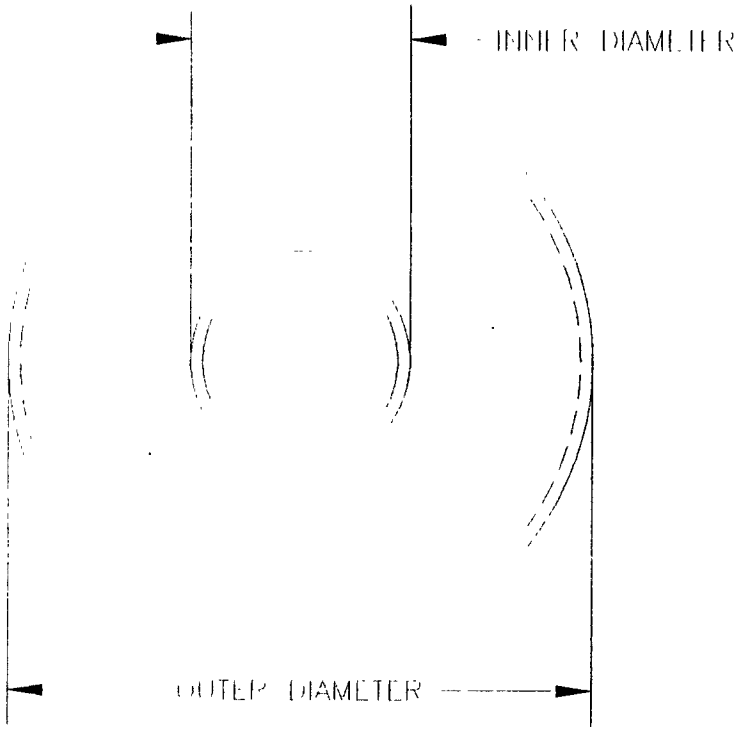

Full Conical Surface

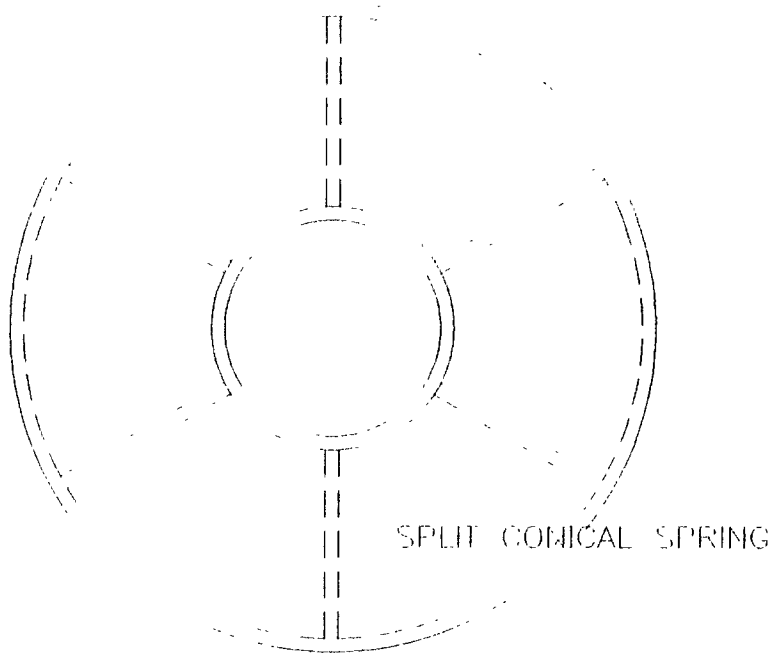

Radial Splits To Reduce Stiffness

CONICAL SPRING CONCEPTS

Design Variables

- Inner And Outer Dia's
- Wall Thickness
- Included Angle Of Conical Shell
- Continuous Double Conical Shell
- Circumferential Split Conical Shell
- Number Of Convolutions
- Number Of Conical Springs/SIS Layer

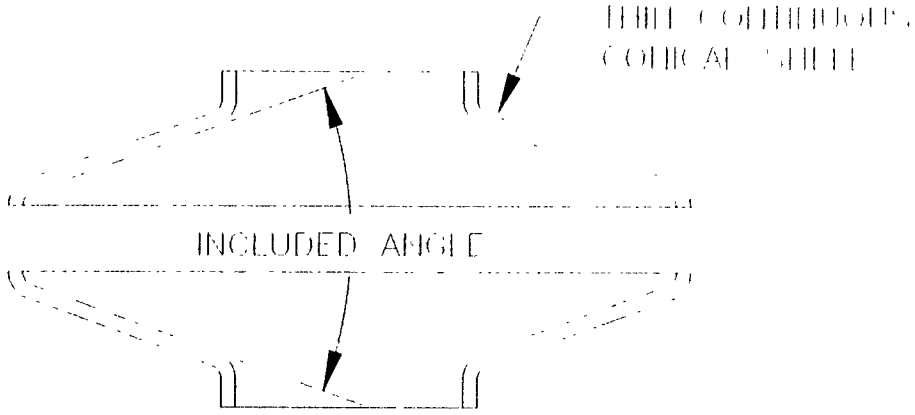

View Of Structure Before Circumferential Seam Weld

Conical Spring Analysis Summary
Finite Element Solutions

OD	ID	T	θ	Conical Shell Condition	Collar Dia	Axial Spring Constant	Bending Spring Constant
cm	cm	cm	deg.		cm	kg/cm	kg-cm/rad
91.2	41.8	.127	10	SPLIT	30	13.1	1875
91.2	41.8	.0635	10	FULL	30	107	
91.2	41.8	.127	10	FULL	30	221	
16.5	6.5	.127	10	FULL	4	731	
14.5	5.4	.127	10	FULL	2	672	
12.5	5.5	.127	10	FULL	1	626	

Conical Spring Analysis Status
Finite Element Solutions

FE Solutions Have Not Covered The Full Parameter Space

- Recommended Size and Stiffness, Both Axial And Bending Must Be Postponed Until Additional Solutions Are Completed
- Preliminary Results Indicate Axial Stiffness Can Be Tailored By Varying Material Thickness, Conical Shell Angle, And General Geometry
- Additional Solutions Would Focus On Strain Produced In The Shell Surface
  - Intent would Be To Maximize Shear Strain Amplitude In The Viscoelastic Constrained Layer

Future Emphasis Must Be Placed On Establishing Bending Stiffness

- Design Information To Be Used In FEA Of Isolation Stack

Static Solution for Split Conical Spring
Beryllium Copper Material

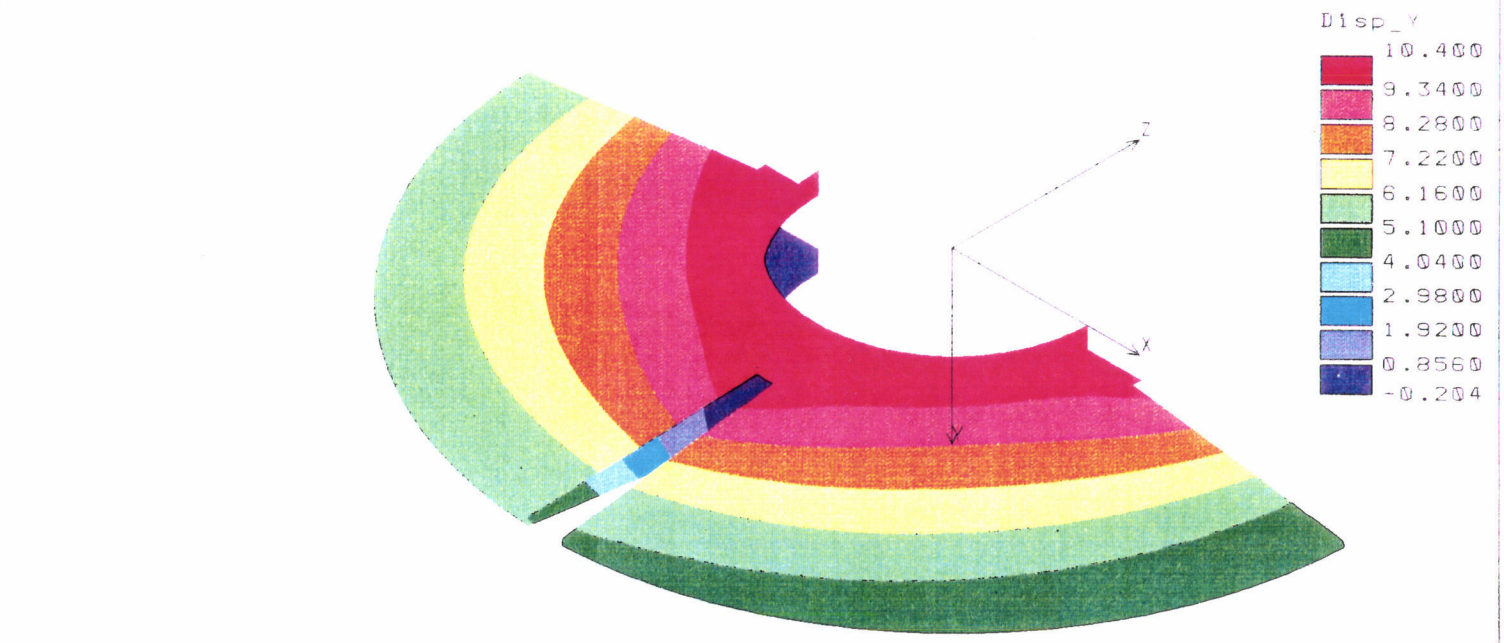

Wall Thickness 0.127 cm
Outer Radius 45.6 cm
Inner Radius 20.9 cm
Collar Radius 15 cm
Load 136 kg
Spring Rate 13.1 kg/cm
Deflection 10.4 cm

Static Solution for Split Conical Spring
Beryllium Copper Material

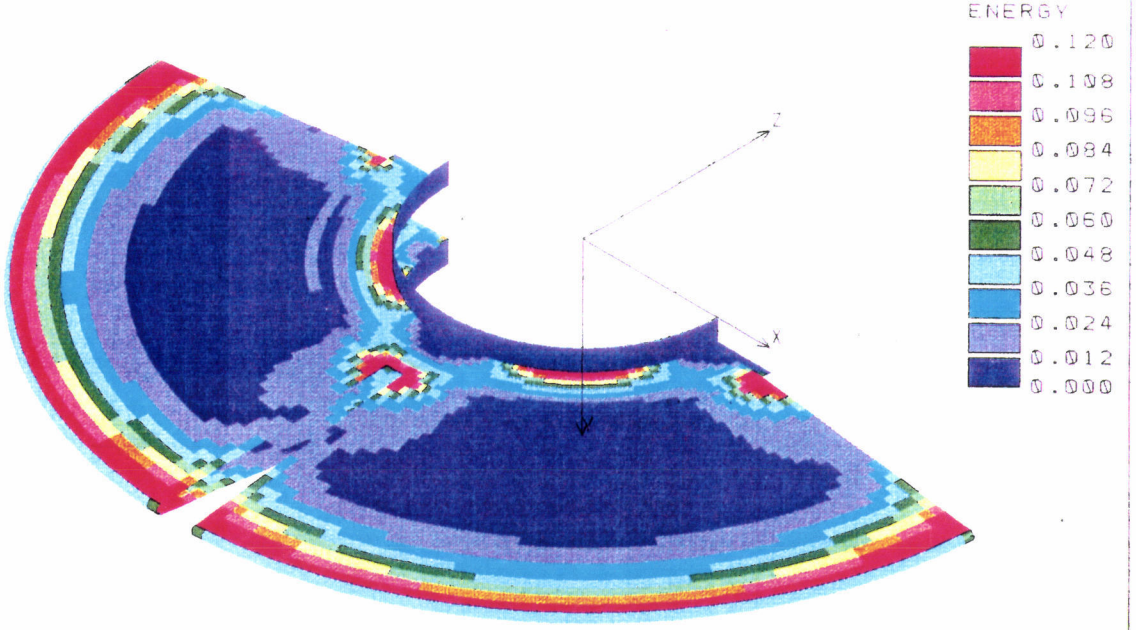

Wall Thickness 0.127 cm
Outer Radius 45.6 cm
Inner Radius 20.9 cm
Collar Radius 15 cm
Load 136 kg
Spring Rate 13.1 kg/cm
Deflection 10.4 cm

Strain Energy Distribution

Stress Solution for Split Conical Spring
Beryllium Copper Material

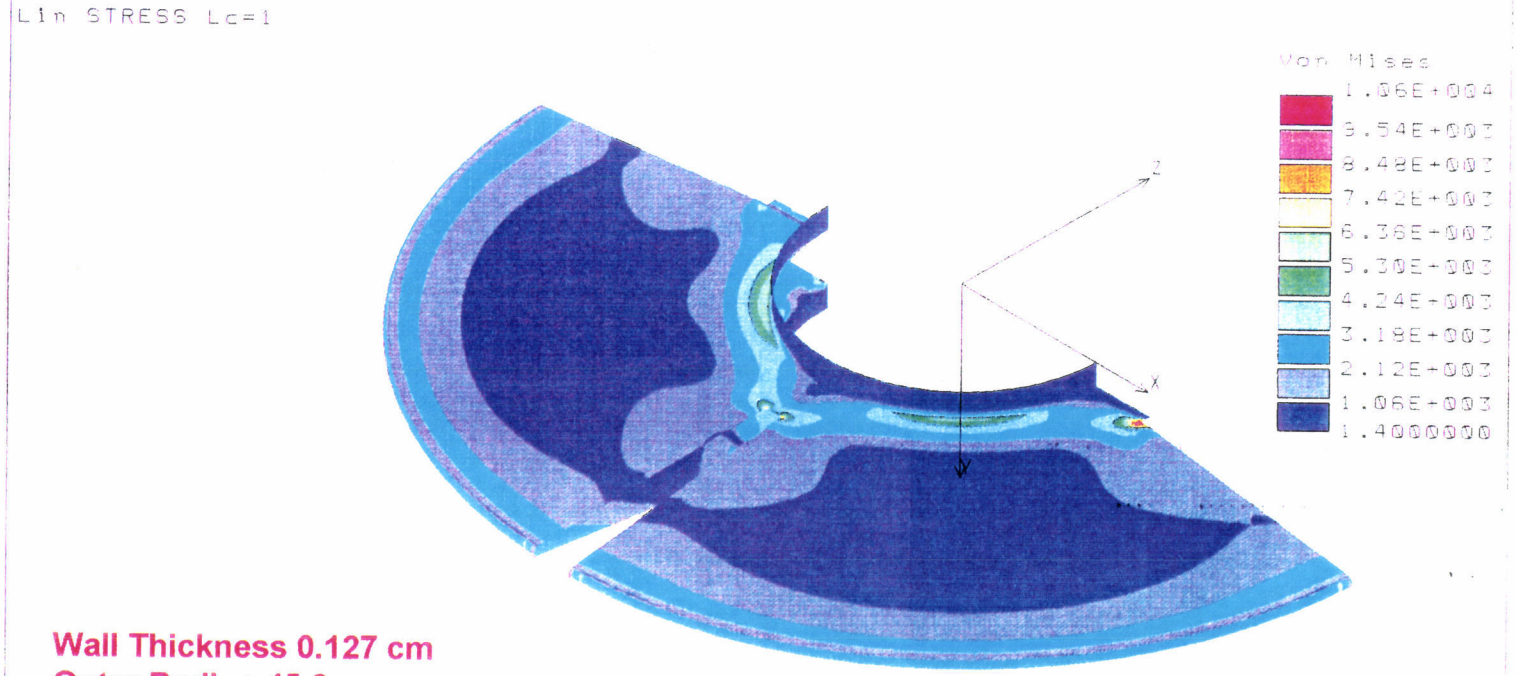

Wall Thickness 0.127 cm
Outer Radius 45.6 cm
Inner Radius 20.9 cm
Collar Radius 15 cm
Load 136 kg
Spring Rate 13.1 kg/cm
Deflection 10.4 cm
Peak Stress 10600 kg/cm^2

Stress Solution for Conical Spring
Beryllium Copper Material

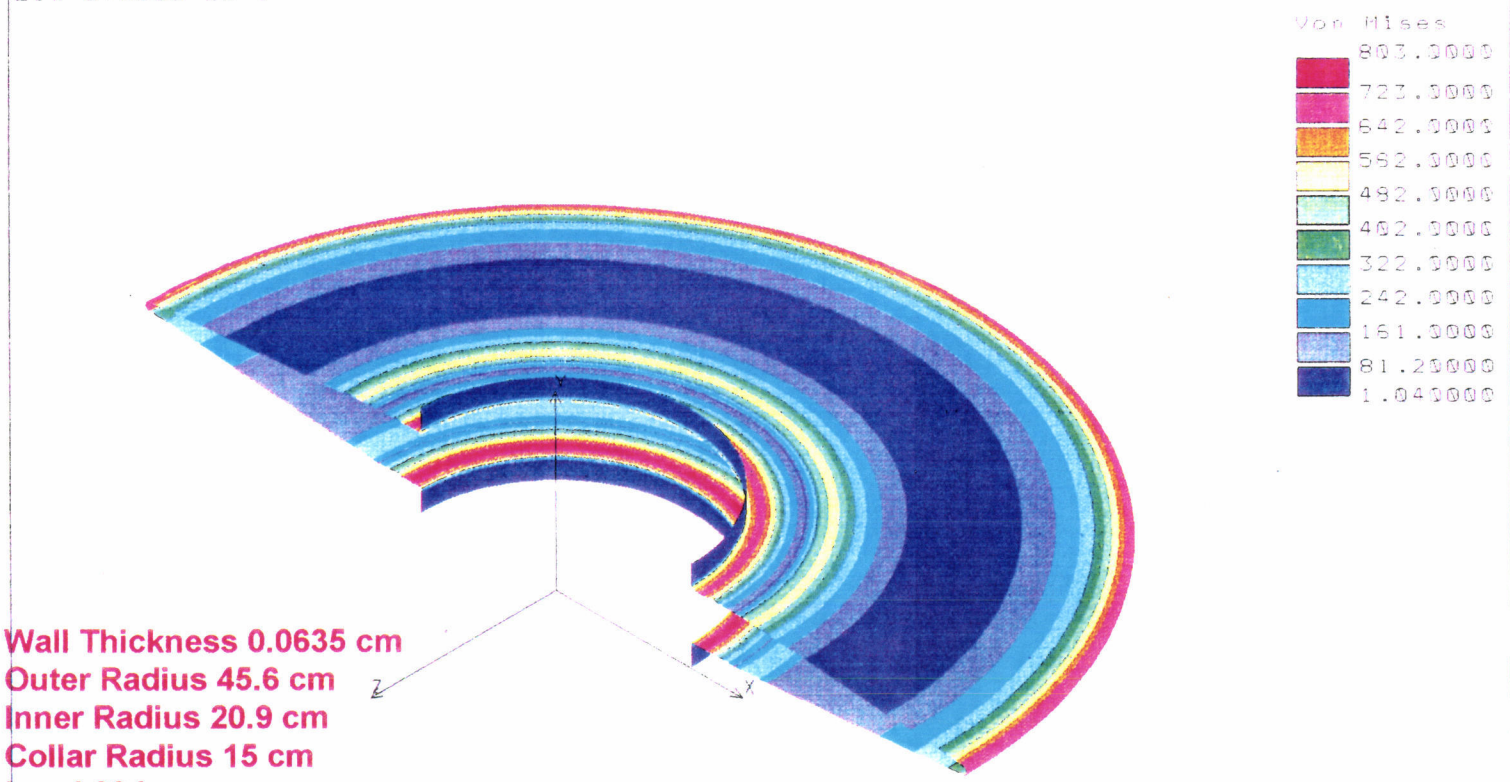

Wall Thickness 0.0635 cm
Outer Radius 45.6 cm
Inner Radius 20.9 cm
Collar Radius 15 cm
Load 66 kg
Stress Peak 803 kg/cm^2
Spring Rate 107 kg/cm
Deflection 0.615 cm

Static Solution for Split Conical Spring
Beryllium Copper Material

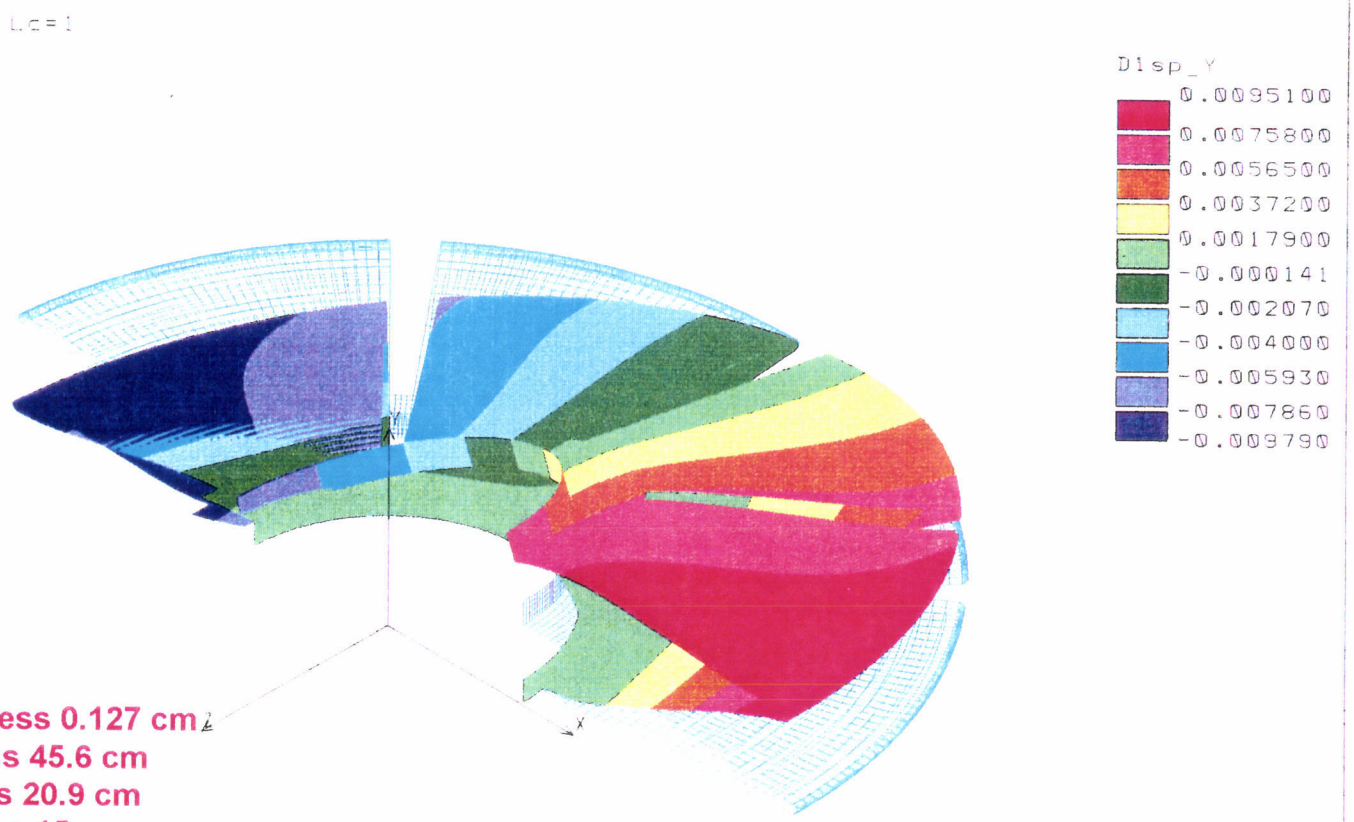

Wall Thickness 0.127 cm
Outer Radius 45.6 cm
Inner Radius 20.9 cm
Collar Radius 15 cm
Load 1 kg-cm Moment
Torsional Spring Rate 1875 kg-cm/rad
Deflection 0.0098 cm

Static Solution for Conical Spring
Beryllium Copper Material

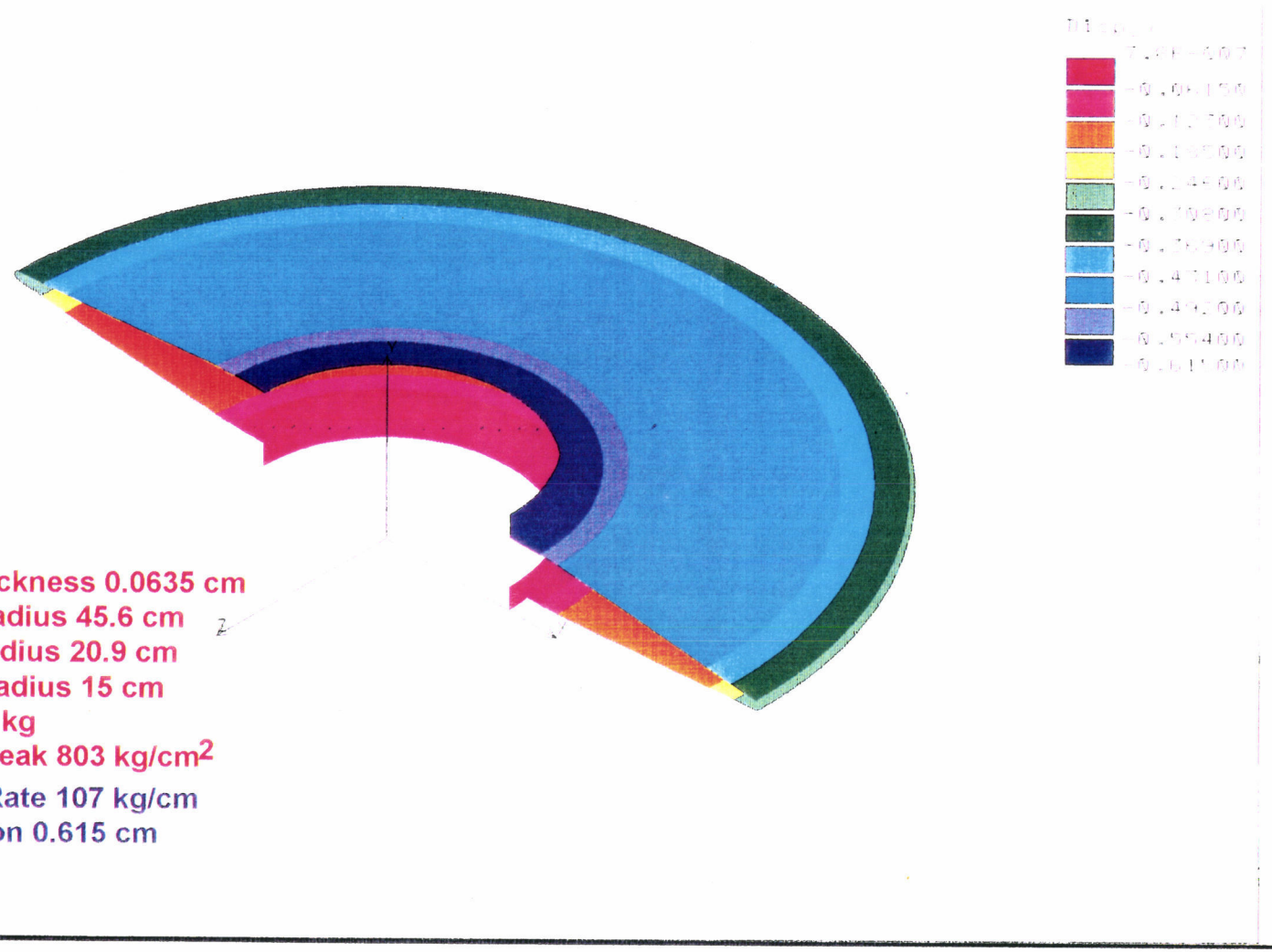

Wall Thickness 0.0635 cm
Outer Radius 45.6 cm
Inner Radius 20.9 cm
Collar Radius 15 cm
Load 66 kg
Stress Peak 803 kg/cm^2
Spring Rate 107 kg/cm
Deflection 0.615 cm

Static Solution for Conical Spring
Beryllium Copper Material

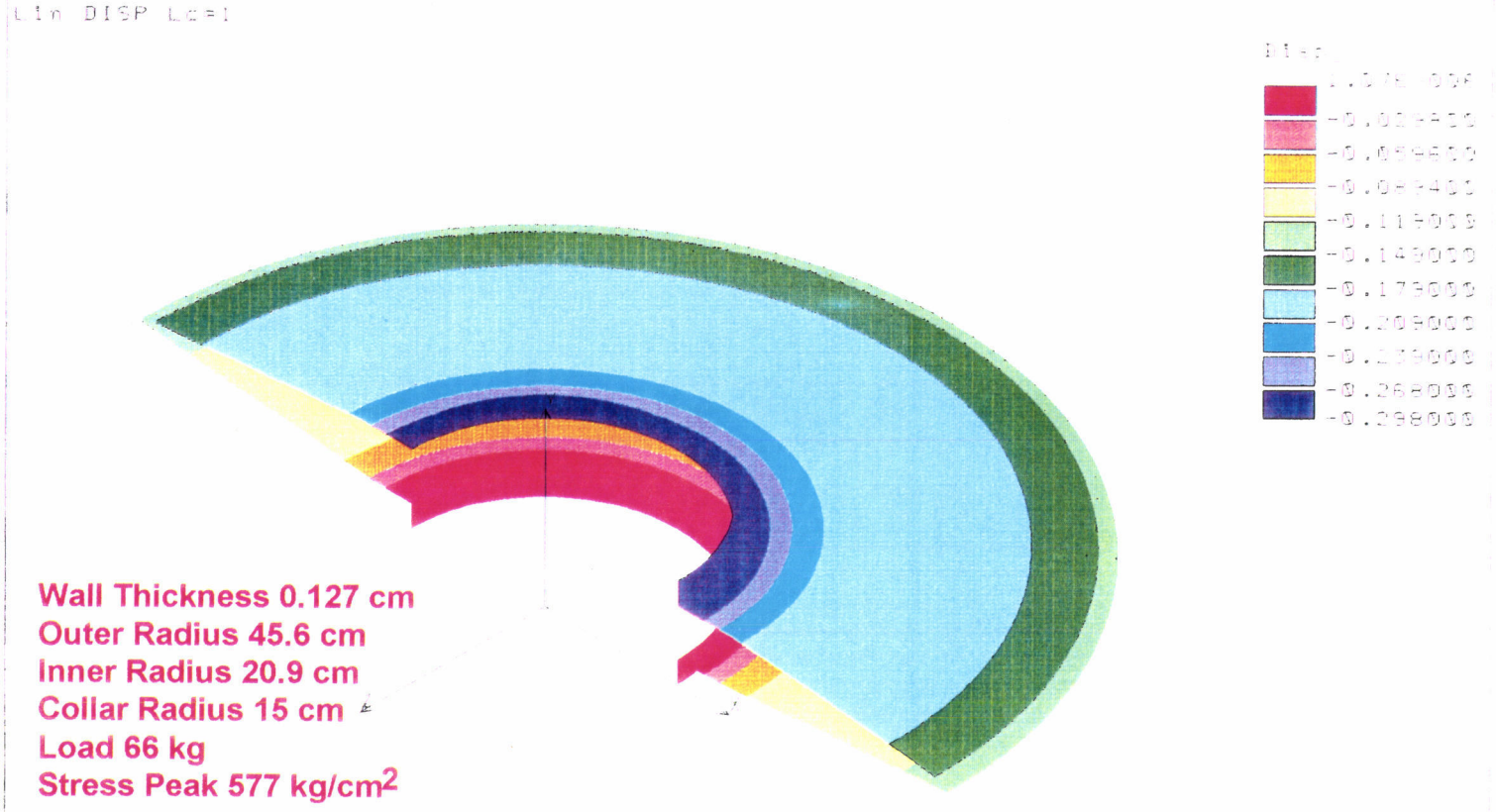

Wall Thickness 0.127 cm
Outer Radius 45.6 cm
Inner Radius 20.9 cm
Collar Radius 15 cm
Load 66 kg
Stress Peak 577 kg/cm^2
Spring Rate 221 kg/cm
Deflection 0.298 cm

Stress Solution for Conical Spring
Beryllium Copper Material

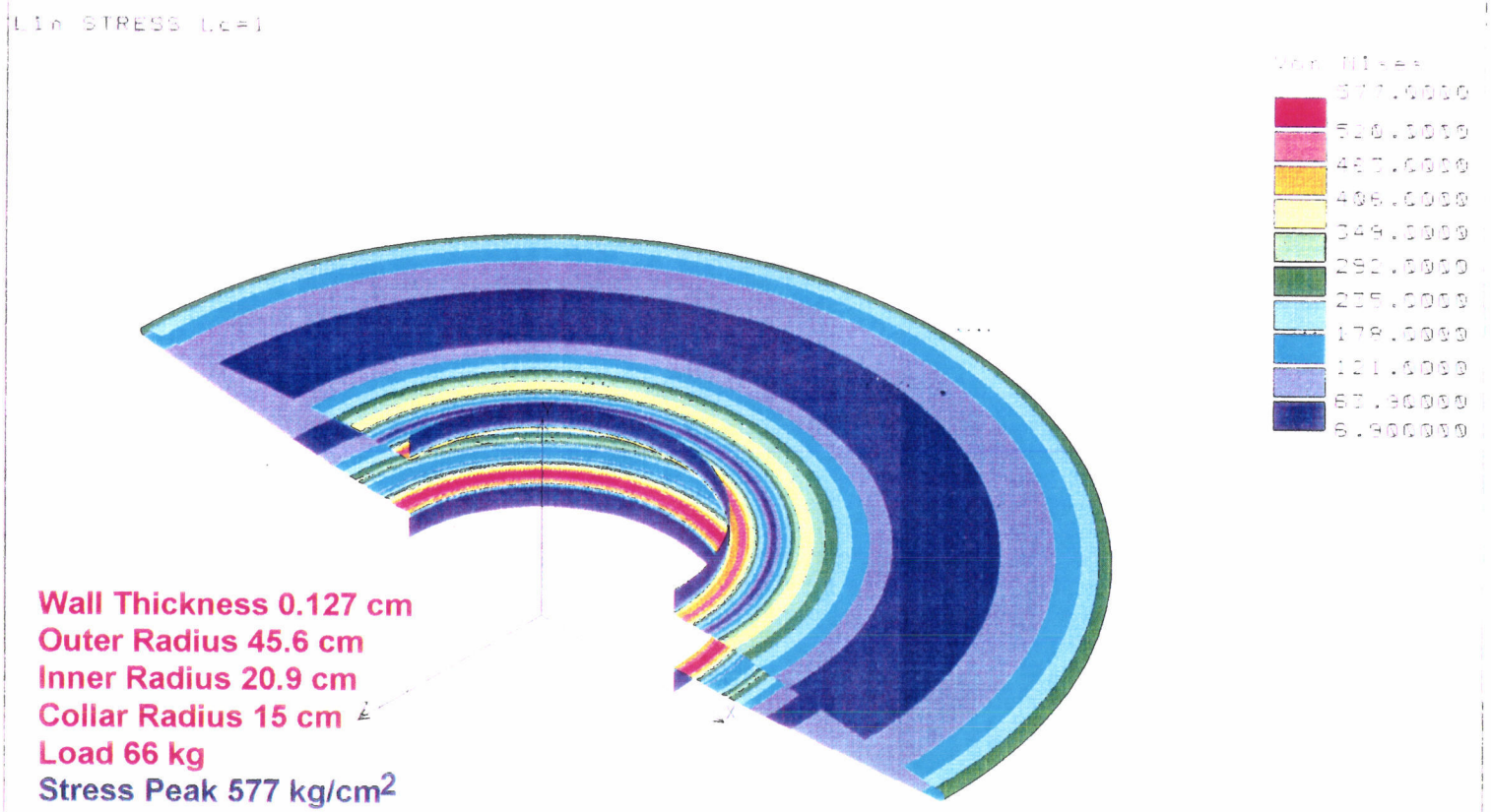

Wall Thickness 0.127 cm
Outer Radius 45.6 cm
Inner Radius 20.9 cm
Collar Radius 15 cm
Load 66 kg
Stress Peak 577 kg/cm^2
Spring Rate 221 kg/cm
Deflection 0.298 cm

Static Solution for Conical Spring
Beryllium Copper Material

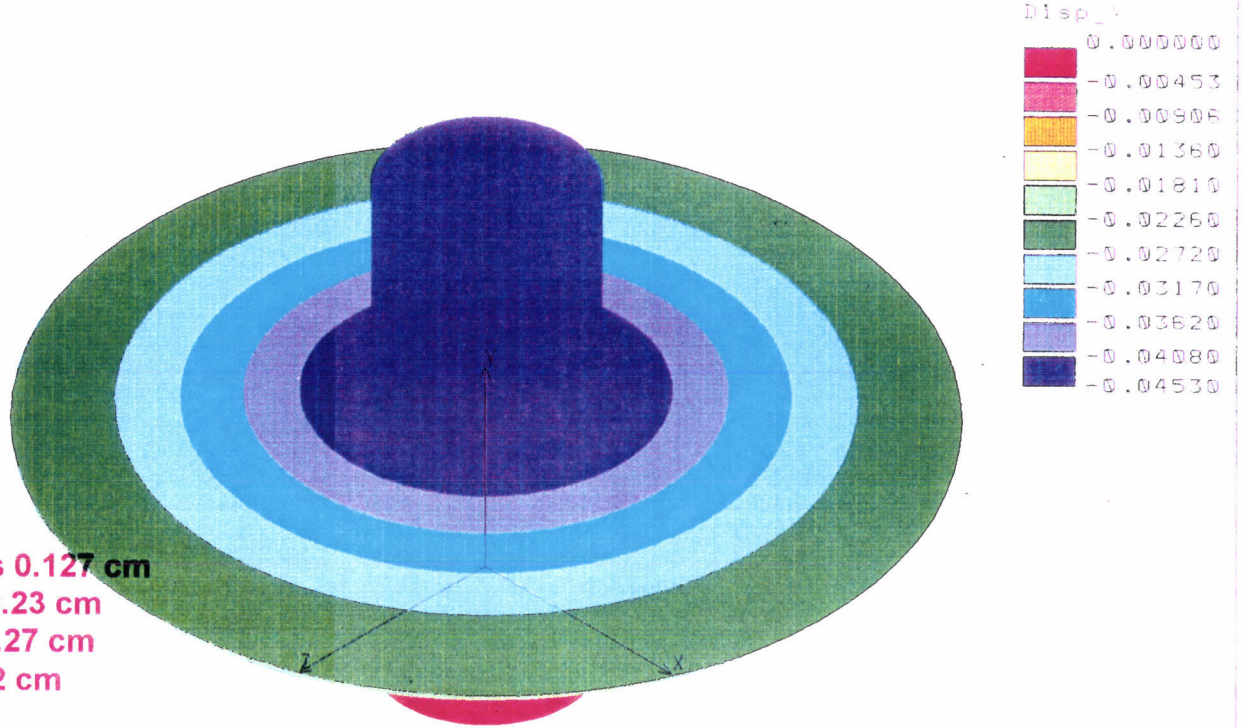

Wall Thickness 0.127 cm
Outer Radius 8.23 cm
Inner Radius 3.27 cm
Collar Radius 2 cm
Load 33 kg
Stress Peak 875 kg/cm^2

Spring Rate 731 kg/cm
Deflection 0.0453 cm

Stress Solution for Conical Spring
Beryllium Copper Material

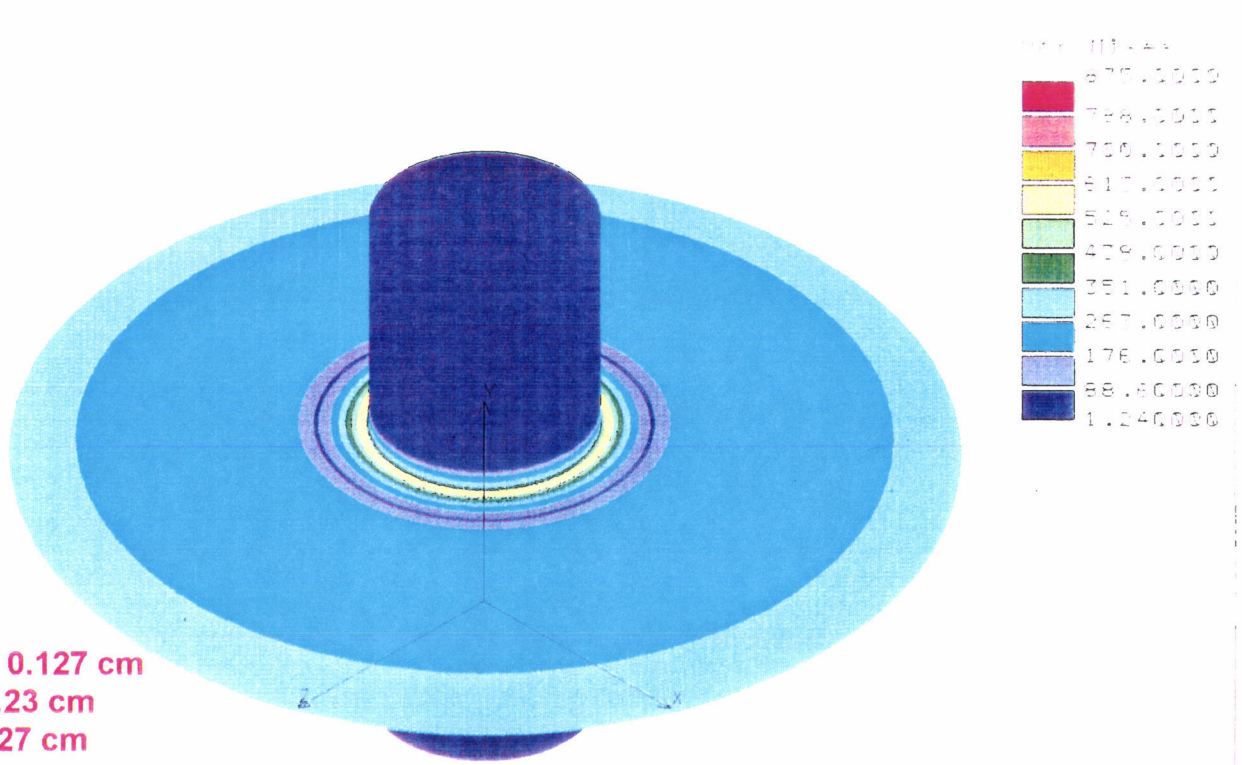

Wall Thickness 0.127 cm
Outer Radius 8.23 cm
Inner Radius 3.27 cm
Collar Radius 2 cm
Load 33 kg
Stress Peak 875 kg/cm^2
Spring Rate 731 kg/cm
Deflection 0.0453 cm

Static Solution for Conical Spring
Beryllium Copper Material

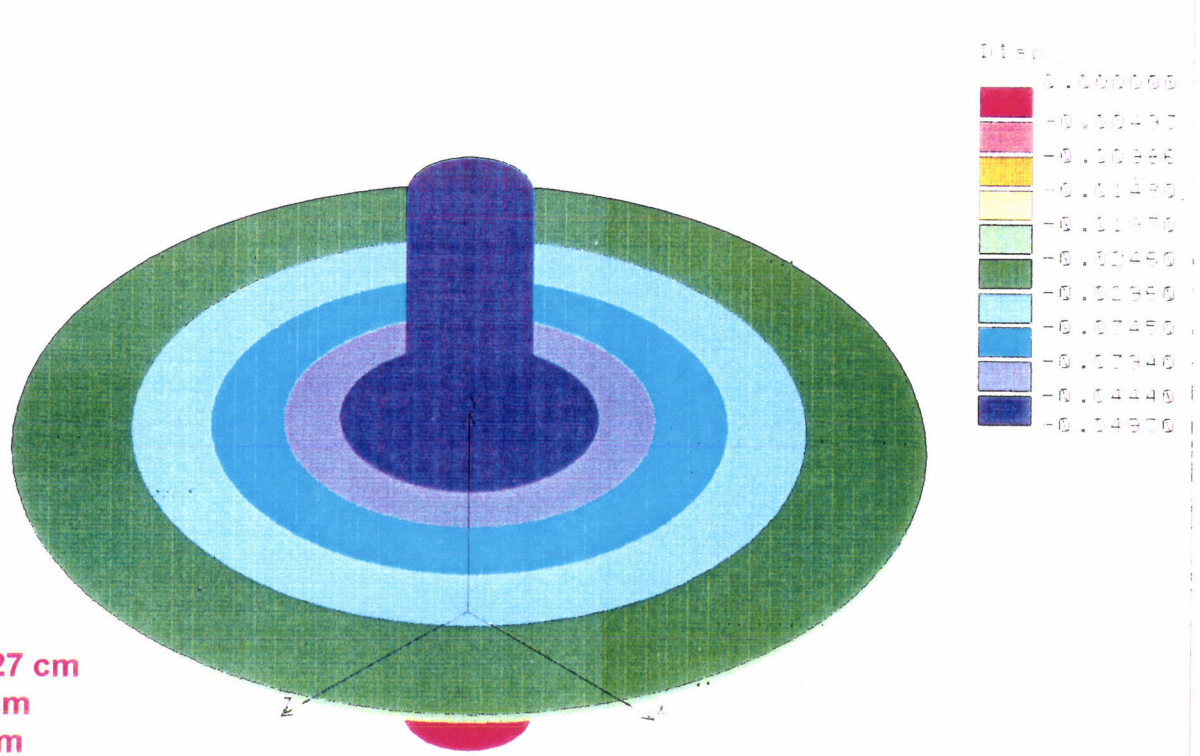

Wall Thickness 0.127 cm
Outer Radius 7.23 cm
Inner Radius 2.27 cm
Collar Radius 1 cm
Load 33 kg
Stress Peak 1305 kg/cm^2
Spring Rate 672 kg/cm
Deflection 0.0493 cm

Stress Solution for Conical Spring
Beryllium Copper Material

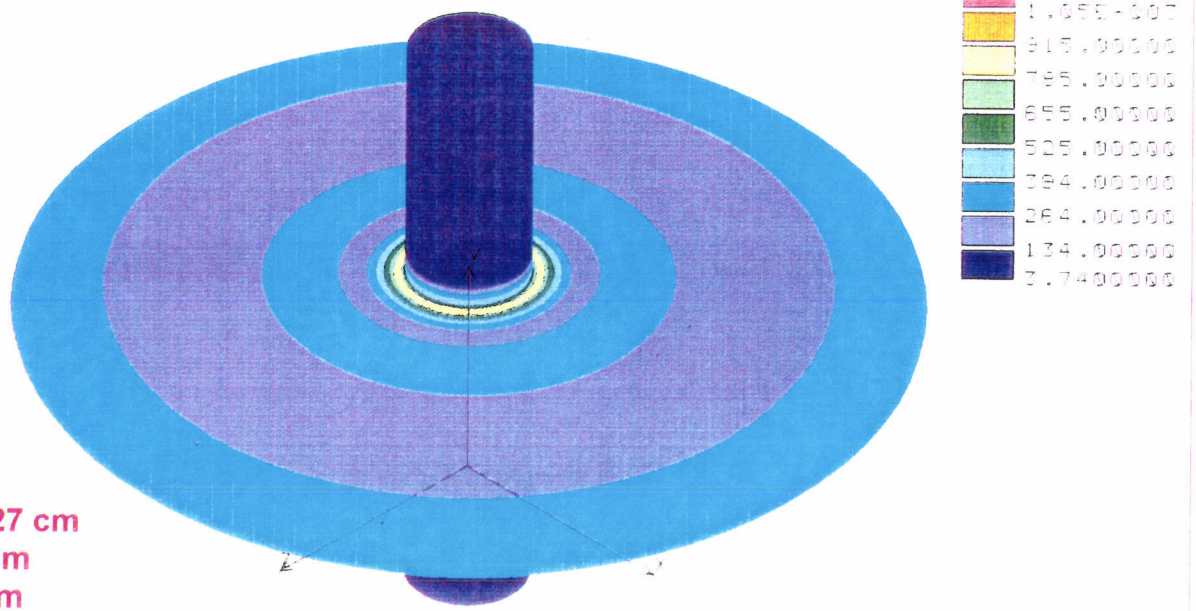

Wall Thickness 0.127 cm
Outer Radius 7.23 cm
Inner Radius 2.27 cm
Collar Radius 1 cm
Load 33 kg
Stress Peak 1305 kg/cm^2
Spring Rate 672 kg/cm
Deflection 0.0493 cm

Static Solution for Conical Spring
Beryllium Copper Material

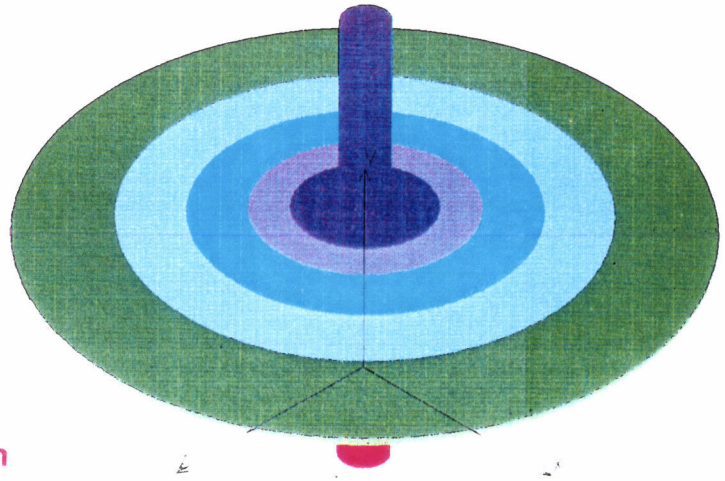

Wall Thickness 0.127 cm
Outer Radius 6.73 cm
Inner Radius 1.77 cm
Collar Radius 0.5 cm
Load 33 kg
Stress Peak 1773 kg/cm^2
Spring Rate 626 kg/cm
Deflection 0.0529 cm

Stress Solution for Conical Spring
Beryllium Copper Material

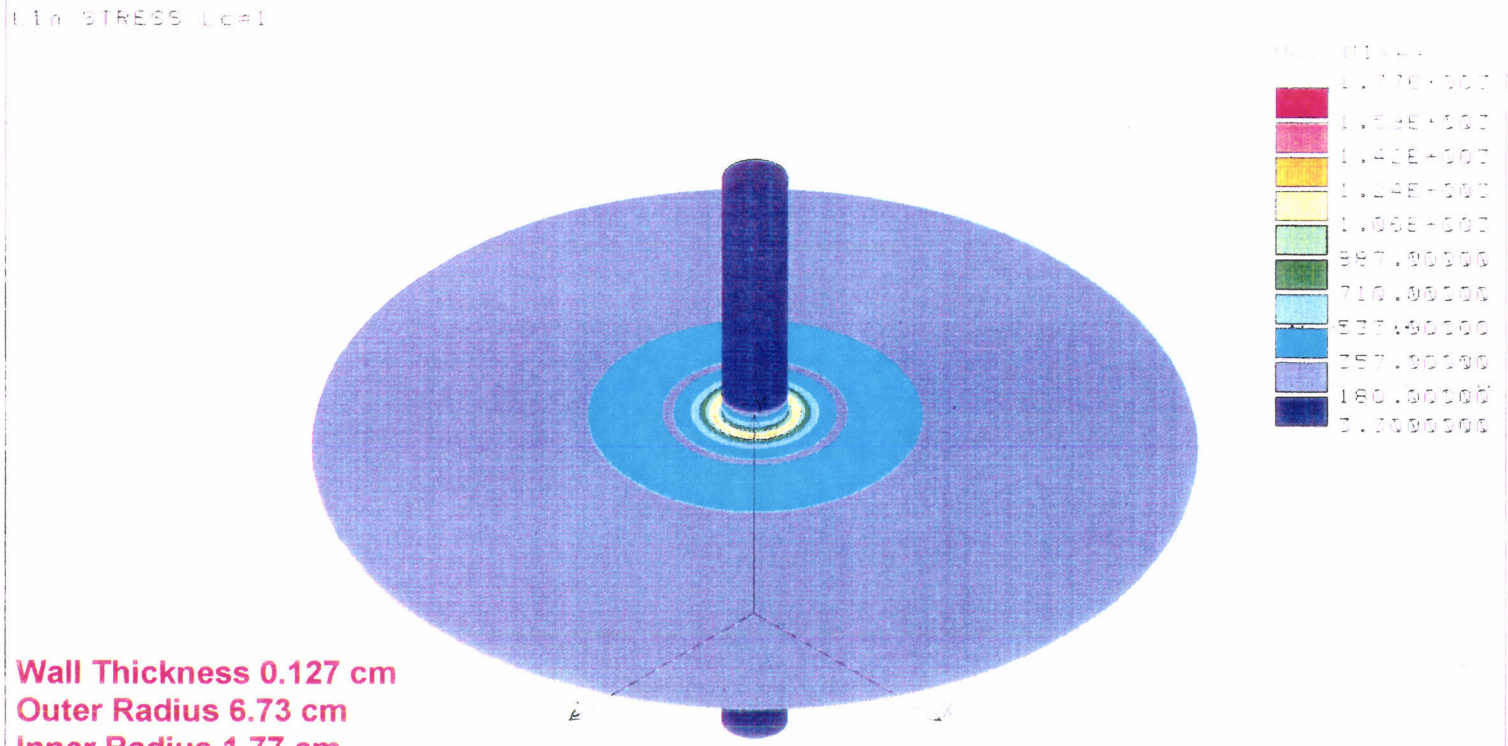

Wall Thickness 0.127 cm
Outer Radius 6.73 cm
Inner Radius 1.77 cm
Collar Radius 0.5 cm
Load 33 kg
Stress Peak 1773 kg/cm^2
Spring Rate 626 kg/cm
Deflection 0.0529 cm

LIGO
Seismic Isolation Stack
Materials Testing

April 28, 1994

W. O. Miller **HYTEC, INC**

Flexural Damping Measurements of Laminated Beryllium-Copper Beams

Work in Progress

Gregory J. Hayman* and John Hanlon†

Los Alamos National Laboratory
29 April, 1994

Introduction

The present study experimentally measures the flexural damping characteristics of laminated beryllium-copper (Be-Cu) beams. These beams are composed of a viscoelastic core, sandwiched between two Be-Cu skins. Composites such as these exhibit high flexural damping capacity, while retaining high flexural rigidity. As a result, the laminates seem promising for use in vibration intolerant environments such as optical equipment or gravitational wave detectors.

While analytical and finite element models have been developed for laminated materials [1-4], the results must be treated with caution, because modeling the viscoelastic material and the viscoelastic material interfaces often presents difficulties. Therefore, an experimental approach is developed to characterize and quantify the flexural damping. The experimental results lend credence to some of the mathematical models.

In this study, we adopt an optical measurement approach, TV holography, for the following reasons: 1) optical methods are capable of characterizing sub-microstrain level damping behavior, 2) TV holography provides full field-of-view results, and 3) the measurements are non-intrusive, allowing actual, application-ready, mechanisms to be studied without having to attach strain gauges or accelerometers to the structure. We intend to achieve a measurement accuracy for the loss factor (η) on the order of 10^{-4}.

We "calibrate" our system by measuring the flexural damping of an aluminum beam. We then measure an individual beryllium-copper skin. Laminated aluminum and Be-Cu beams were then tested, and the damping characteristics are compared with the solid material samples. The laminates showed superior damping capacity as compared with the solid beams, and the Be-Cu laminate showed slight improvements over the aluminum laminate.

---

* Graduate Research Assistant
† Staff Member

TV Holography Measurement Systems

General

TV holography (TVH) is a useful, sensitive tool to verify the mechanical stability and dynamic characteristics of prototype structures. TVH is a noncontact, full field-of-view interferometric method for measuring the shape changes of non optical parts due to a variety of effects such as thermal heating and mechanical stress, and the dynamic characteristics of mechanical systems, such as mode shapes and mode frequencies. Often, a stated goal of stability testing is to compare predictions from finite element models (FEM) used for design, with the properties of mechanical prototypes. Since TVH provides full field-of-view, "real time" (TV frame rate) measurements with submicron sensitivity, it often shows features that were not predicted by FEM. The differences between models and test results lead to better understanding, ideas for improved designs, and better modeling techniques.

TVH systems have been researched since the 1970's, but faster, smaller computers and a phase shifting technique for directly evaluating speckle intensity patterns, make TVH in the 1990's, a very useful measurement tool for many applications. The present trend in TVH system development is to build smaller systems for use outside of controlled laboratory environments with vibration isolation tables, and to develop more robust algorithms to quickly calculate and display surface shape changes from fringe data. The newest systems measure 3D shape changes, in-plane or out-of-plane shape change components and dynamic characteristics.

Los Alamos has several TVH systems. Two of our systems have 30 Hz, "real time" capability, and we have developed efficient, robust image processing algorithms using an interactive code written in IDL (Interactive Data Language), to process fringe data into surface shape plots. We are developing systems that use common path interferometers for more robust laboratory measurement systems.

Basic Principles

Layout

A typical TVH system layout is shown in **Figure 1.** One beam, called the reference beam, is reflected from a mirror mounted on a piezoelectric pusher and then expanded and directed toward the CCD camera. The other beam is expanded and directed toward the object. Light scattered by the object is collected by a zoom lens that images the object onto the CCD camera

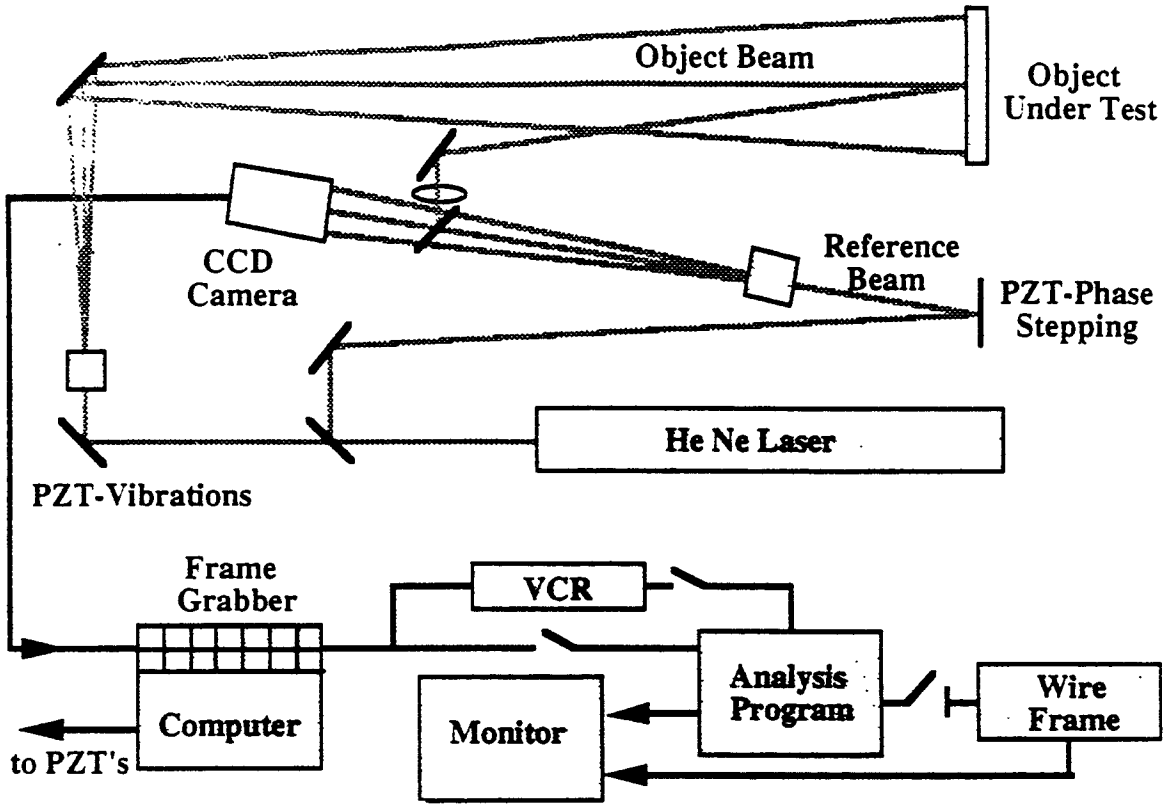

Figure 1 A typical TV holography layout

Shape Change Measurements

A shape change measurement typically involves collecting and processing 8 frames of camera data. Four frames are gathered from the object in an initial or "start" state. The other 4 frames are collected after the object is deformed. In each state, 4 frames are gathered sequentially. Between each frame in the 4 frame set, the piezoelectric pusher in the reference beam is moved to change the path length by a quarter wavelength of light. This is called phase stepping. Processed information is sent to the TV monitor, which displays fringes representing the shape change caused by the load. The fringe pattern is superimposed over the image of the object. Modern image processors display the data at the TV frame rate. Shape changes that are slow compared to TV frame rates are observed in "real time".

For the object "start" state, the i^{th} frame intensity at each CCD camera pixel locations is described by the equation for two beam interference:

$$I_i(x_p,y_p) = I_O + I_r + 2\sqrt{I_O I_r}\cos[\phi_O - \phi_r].$$

The o and r subscripts refer to the object and reference beams, and the pair (xp,yp) refers to the location of pixel p. The optical phases ϕ_O and ϕ_r are proportional to the path

lengths of the object and reference beams from the first beam splitter to the CCD camera. After the part deforms, the pixel intensity for the j^{th} frame is given by:

$$I_j'(x_p,y_p) = I_O + I_r + 2\sqrt{I_O I_r}\cos[(\phi_O + \Omega) - \phi_r].$$

The phase shift Ω is related to the optical path length change caused by part deformation; Ω contains the shape change information. The phase Ω is separated from the 3 other unknowns, I_O, I_r, and $[\phi_O - \phi_r]$, by phase stepping the piezoelectric pusher in the reference beam between each frame, with phase steps of 0, $\pi/2$, π, and $3\pi/2$. The 4 frame intensities for the "start" state are given by:

$$I_1(x_p,y_p) = I_O + I_r + 2\sqrt{I_O I_r}\cos[\phi_O - \phi_r].$$
$$I_2(x_p,y_p) = I_O + I_r + 2\sqrt{I_O I_r}\cos[\phi_O - \phi_r - \pi/2]$$
$$I_3(x_p,y_p) = I_O + I_r + 2\sqrt{I_O I_r}\cos[\phi_O - \phi_r - \pi]$$
$$I_4(x_p,y_p) = I_O + I_r + 2\sqrt{I_O I_r}\cos[\phi_O - \phi_r - 3\pi/2]$$

After the object moves, the 4 frame intensities are:

$$I_1'(x_p,y_p) = I_O + I_r + 2\sqrt{I_O I_r}\cos[\phi_O - \phi_r + \Omega]$$
$$I_2'(xp,yp) = I_O + I_r + 2\sqrt{I_O I_r}\cos[\phi_O - \phi_r + \Omega - \pi/2]$$
$$I_3'(x_p,y_p) = I_O + I_r + 2\sqrt{I_O I_r}\cos[\phi_O - \phi_r + \Omega - \pi]$$
$$I_4'(x_p,y_p) = I_O + I_r + 2\sqrt{I_O I_r}\cos[\phi_O - \phi_r + \Omega - 3\pi/2]$$

If $D_1 = (I_1 - I_3) + (I_1' - I_3')$ and $D_2 = (I_2 - I_4) + (I_2' - I_4')$,

then the monitor display:

$$D_1^2 + D_2^2 = 32 I_O I_r(1 + \cos[\Omega]),$$

shows fringes draped over the object. More frame grabber arithmetic leads to an expression for Ω. The arithmetic is easy. Let

$$N_1 = (I_1 - I_3) + (I_2' - I_4') \qquad D_1 = (I_1 - I_3) + (I_1' - I_3')$$
$$N_2 = (I_2 - I_4) - (I_1' - I_3') \qquad D_2 = (I_2 - I_4) + (I_2' - I_4')$$
$$N_3 = (I_1 - I_3) - (I_2' - I_4') \qquad D_3 = (I_1 - I_3) - (I_1' - I_3')$$
$$N_4 = (I_2 - I_4) + (I_1' - I_3') \qquad D_4 = (I_2 - I_4) - (I_2' - I_4')$$

and let

$$N = (N_1^2 + N_2^2) - (N_3^2 + N_4^2) = 64\, I_O I_r \sin[\Omega]$$
$$D = (D_1^2 + D_2^2) - (D_3^2 + D_4^2) = 64\, I_O I_r \cos[\Omega]$$

then,

$$\Omega = atan[N/D]$$

Once Ω is known, the shape change between the deformed and the reference state of the object is calculated. The arctangent calculation of Ω provides information modulo

2π, which is called phase wrapped data. Finding and taking out the 2π phase jumps is called phase unwrapping. Unwrapping would be simple if the data were clean, but scattered laser light has speckle noise, which makes unwrapping difficult; however, recently developed unwrapping algorithms have quite good noise immunity. The dynamic range of shape change can be extended if the process that causes the change is slow enough by taking a new base state before the fringe spacing gets to dense. The shape change form this new base state is added to the shape change from the first base state after the test is complete.

Dynamic Measurements

The same TVH system optical layout is used for dynamic measurements, but the processing algorithm is different. A technique used to display mode shapes of vibrating parts is called time average holography. In time average holography the phase W, which contains the mode shape information, is a function of time and position along the part. For example, for a cantilever beam vibrating at a frequency ω,

$$W[x,t] = 2kD[x]\cos[\omega t],$$

where D[x] is the maximum displacement amplitude at position x, from the cantilever base. At each CCD pixel the intensity is given by:

$$I[x,t] = I_O + I_r + 2\sqrt{I_O I_r}\cos[f_O - f_r + 2kD[x]\cos[\omega t]]$$

If the camera frame time is much longer than the cantilever oscillation period, a camera frame records a time average of the intensity which is given by:

$$< I[x,t] > = I_O + I_r + 2\sqrt{I_O I_r}\cos[f_O - f_r]\, J_O^2[2kD[x]] == I_j$$

where J_O is the 0-order Bessel function. Four phase shifted frames (I_j) are collected and processed according to:

$$(I_1 - I_3)^2 + (I_2 - I_4)^2 = 16 I_O I_r J_O^2[2kD[x]]]$$

When the processed information is displayed on the TV monitor, the fringes are a contour map of the mode shape for the vibrating part.

Examples

Several examples of static and dynamic mode TVH results are shown below. The first result shows the effect of twisting, buckling and hand heating a silicon cantilever. The cantilever was made from 4 pieces of engineering grade silicon 34 mm and 60-mm long. The silicon pieces are butt-bonded together to make a ladder 240 mm long by 34 mm wide and 300 μm thick. Down the length of each side of the ladder, 4 mm wide and 200 μm thick graphite epoxy strips are bonded to the silicon to stiffen the part. For the tests, a ladder is bonded to the top and bottom sides of two graphite blocks, and this assembly is

mounted to precision rotation and translation stages. With this mechanical arrangement the ladder can be twisted, stretched, compressed or hand heated. The results are shown in **Figure 2.** Each fringe spacing corresponds to approximately $\lambda/2 = 0.32\ \mu m$ of shape change.

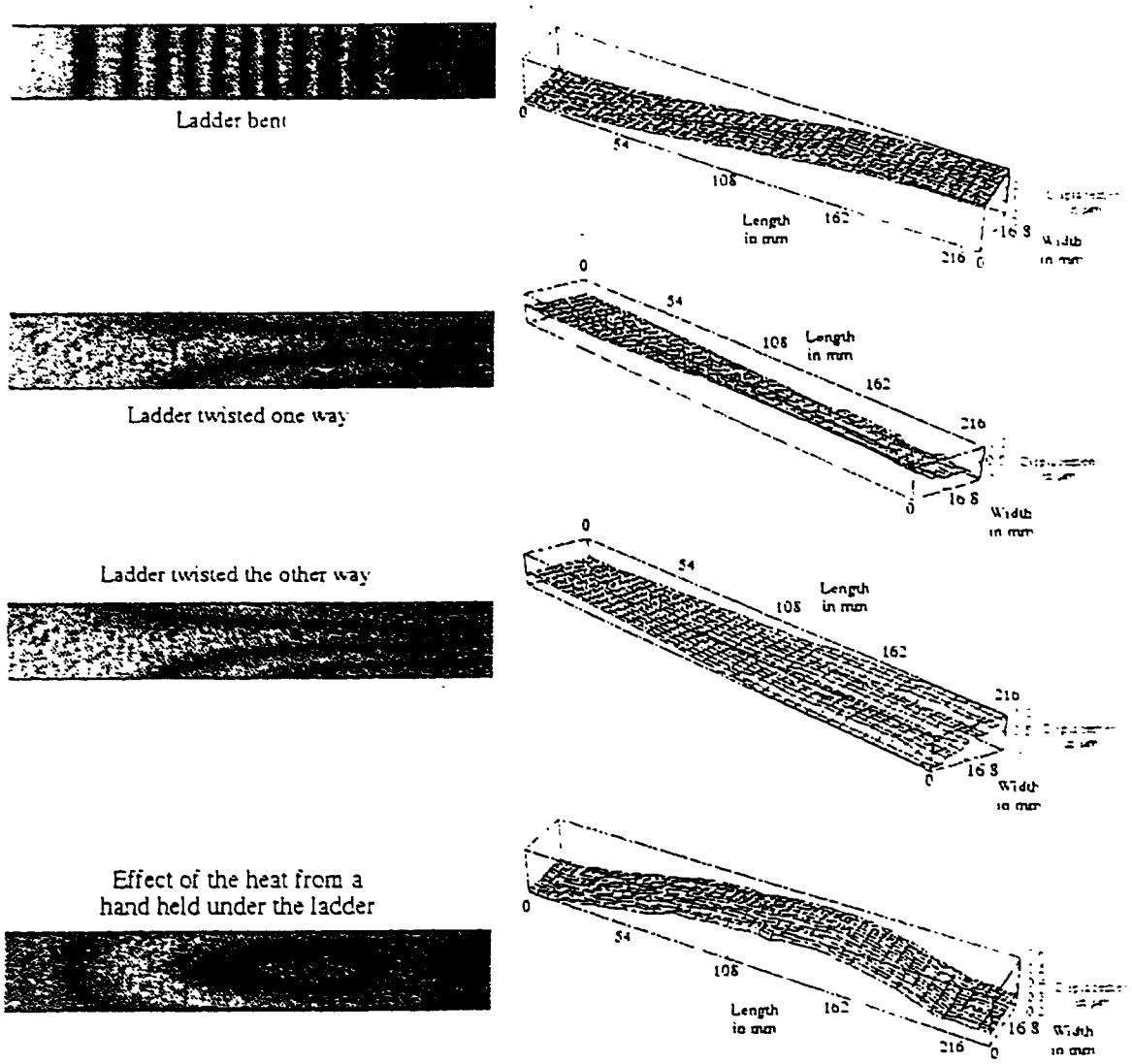

Figure 2 Results showing the effects of twisting, buckling, and hand heating a silicon cantilever.

Dynamic mode shapes of silicon cantilevers are shown in **Figure 3** and **Figure 4.** These figures show several vibration modes for the mounted in different configurations and with and without the stiffing ribs along the sides of the cantilever. These figures show what is possible and the technique we attempted to apply to measure the damping coefficient of the beams for this report.

A recent example of our improved unwrapping algorithm is shown in **Figures 5**

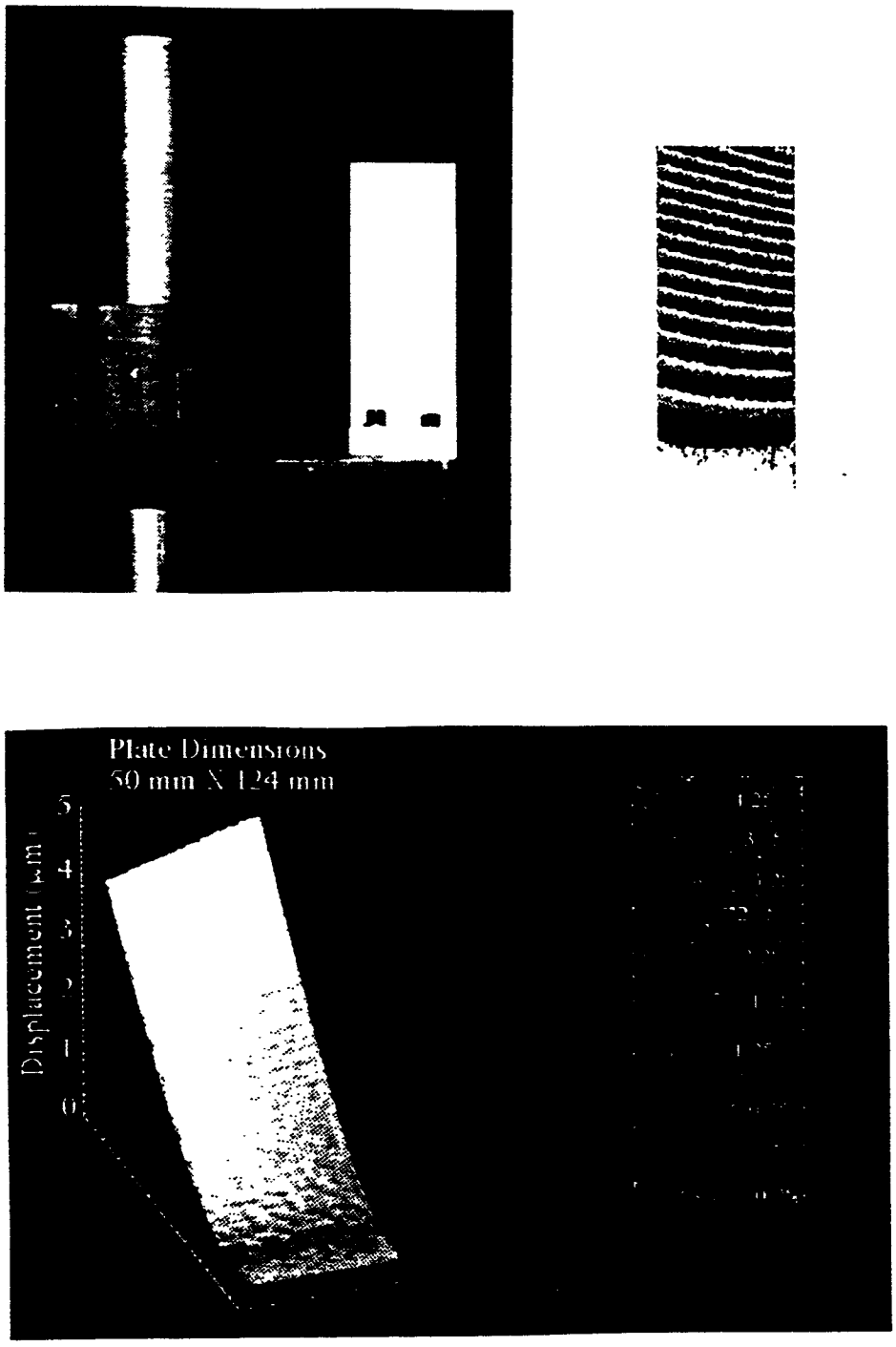

Figure 5 An example of results from our improved fringe unwrapping algorithm. The setup, the fringe pattern and the processed surface shape are shown.

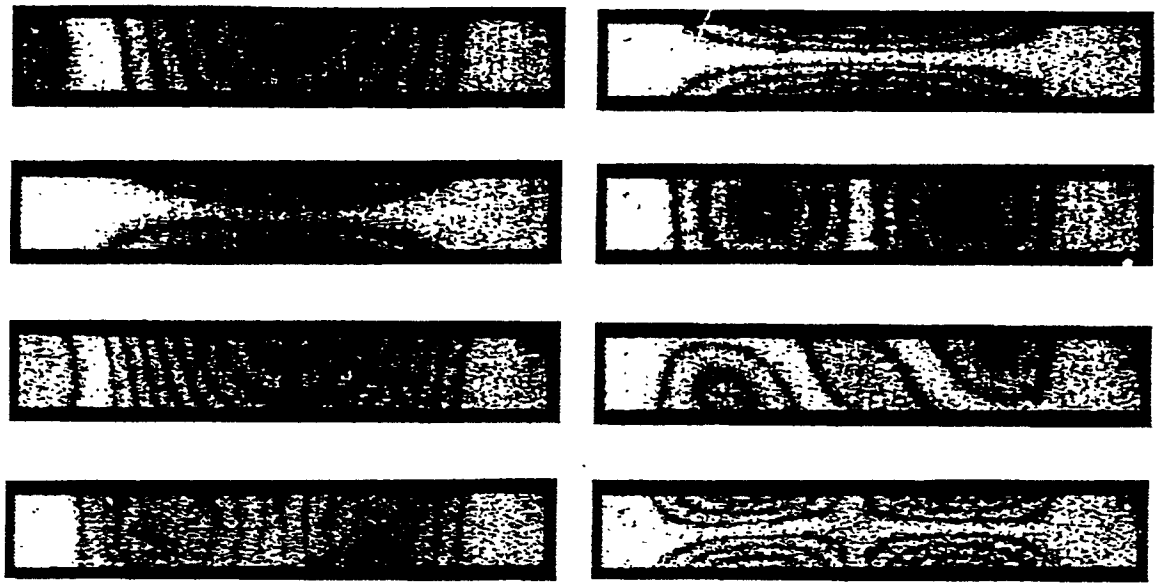

Figure 3 Fringe patterns mode shapes for a vibrating silicon part supported near each end.

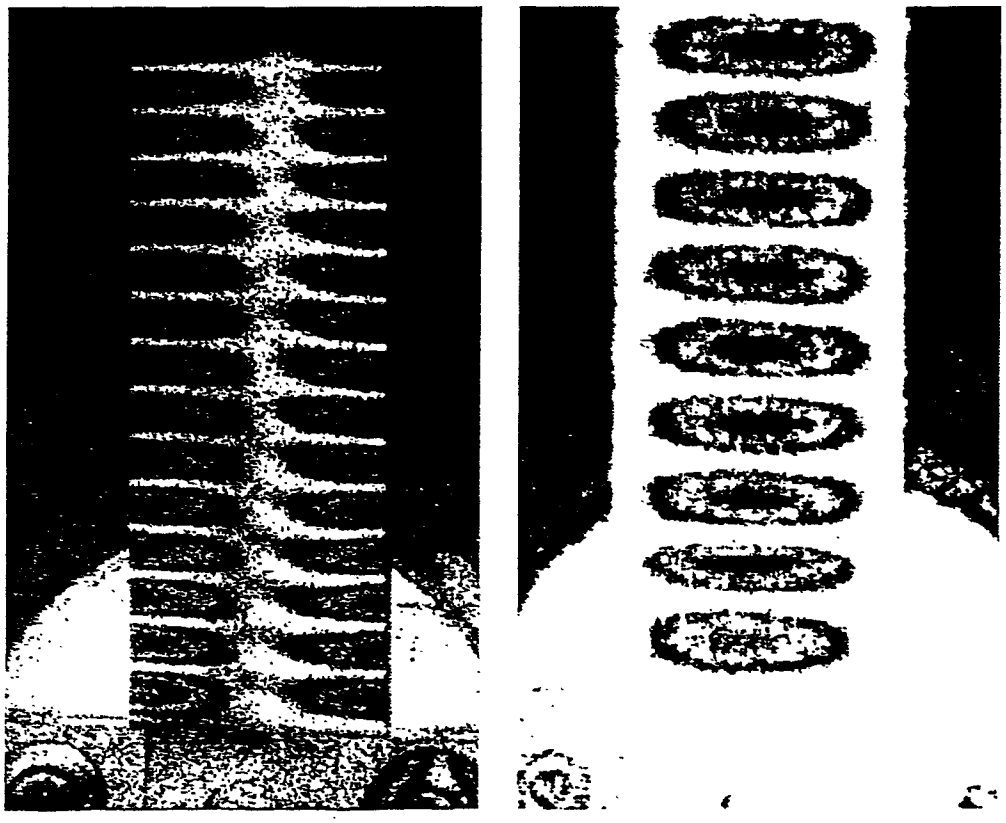

Figure 4 Mode shapes of silicon cantilever with and without graphite stiffening strips along the side.

Conclusion

TV holography is full field of view testing method that provides essential information about prototype parts with submicron sensitivity in realistic test configurations. TVH is capable of providing understanding about stability and vibration questions that cannot be answered by FEM modeling alone. State of the art TVH systems update at 30 Hertz, and can be small if single frequency lasers are used for illuminating the object. The software to unwrap fringes produces quantitative 3-D surface plots of the surface shape.

Experimental Procedure

Testing Apparatus

The test samples were excited with a piezoelectric shaker assembly which produced a nominal .24 μm of axial displacement per 100 volts of input and had an operating range up to 150 kHz. The shaker was mounted to a bulky aluminum support whose resonances were outside the frequency range of this study. We attached the sample to the face of the piezoelectric shaker with a simple sandwich clamp. The sample was placed between the clamp, and then the whole assembly was tightened down onto the face of the shaker using two 1/4 inch bolts. The shaker/clamp assembly, along with a clamped sample, is shown in **Figure 6**. We believed this assembly would provide the desired boundary conditions for the analysis of a cantilevered beam.

A Wavetek model 650 wave generator was used to supply the input signal to the shaker. Before reaching the shaker, the signal could be amplified using Techtron 7570 power amplifier. With this configuration we could excite the shaker from dc--150 kHz with an amplitude of 0--200 Vpp.

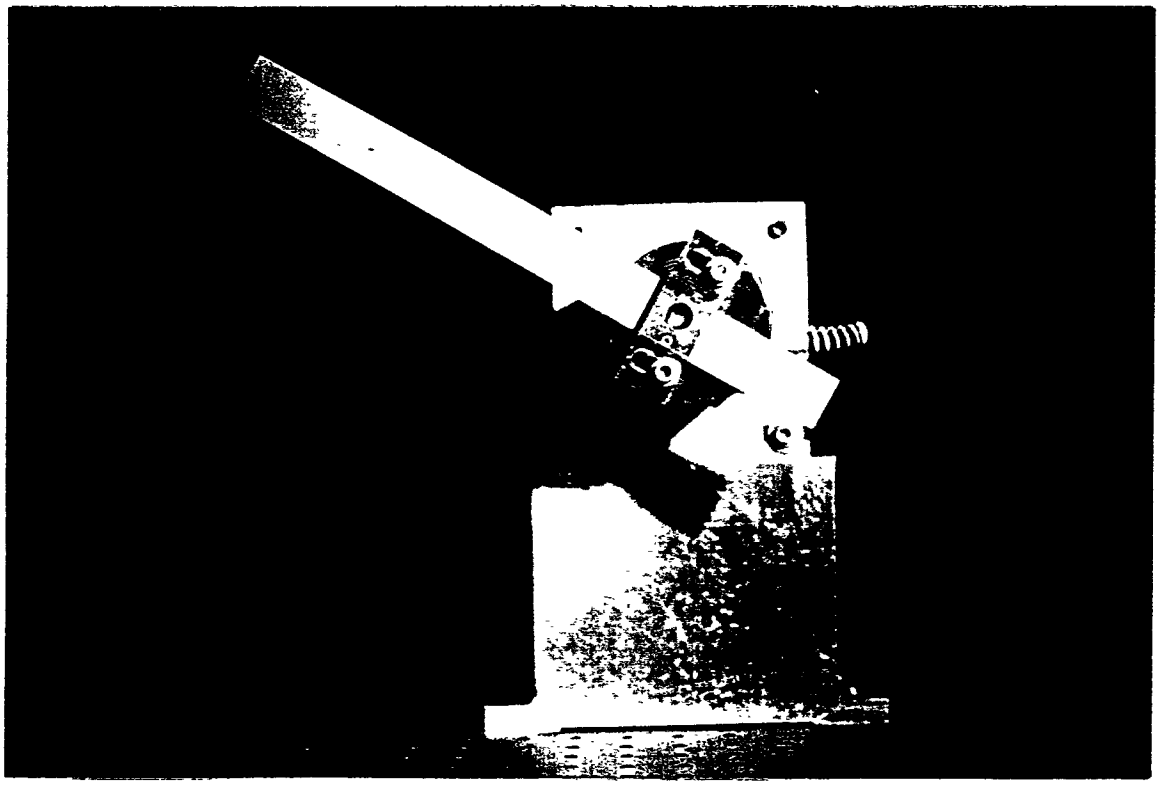

Figure 6 Experimental testing apparatus showing a clamped sample, the piezoelectric shaker, and the main support.

Damping Measurements

We examined the material's flexural damping in terms of loss factor (η), which is defined as:

$$\eta = \frac{\omega_2 - \omega_1}{\omega_n}$$

Here, ω_n is the resonance frequency and ω_1, ω_2 are the half power points along the resonance curve.

With the sample clamped in the testing apparatus, we drove the piezoelectric shaker until a resonance fringe pattern was observed on the monitor of the TVH system. **Figure 7** shows a typical fringe pattern for the cantilevered samples. We recorded both ω_n and the amplitude of the resonance vibration. We then located the half power points, ω_1, ω_2, by changing the excitation frequency and observing the resulting fringe pattern. We introduce some measurement inaccuracy by using visual interpretation of the fringe patterns to obtain ω_n, ω_1, and ω_2.

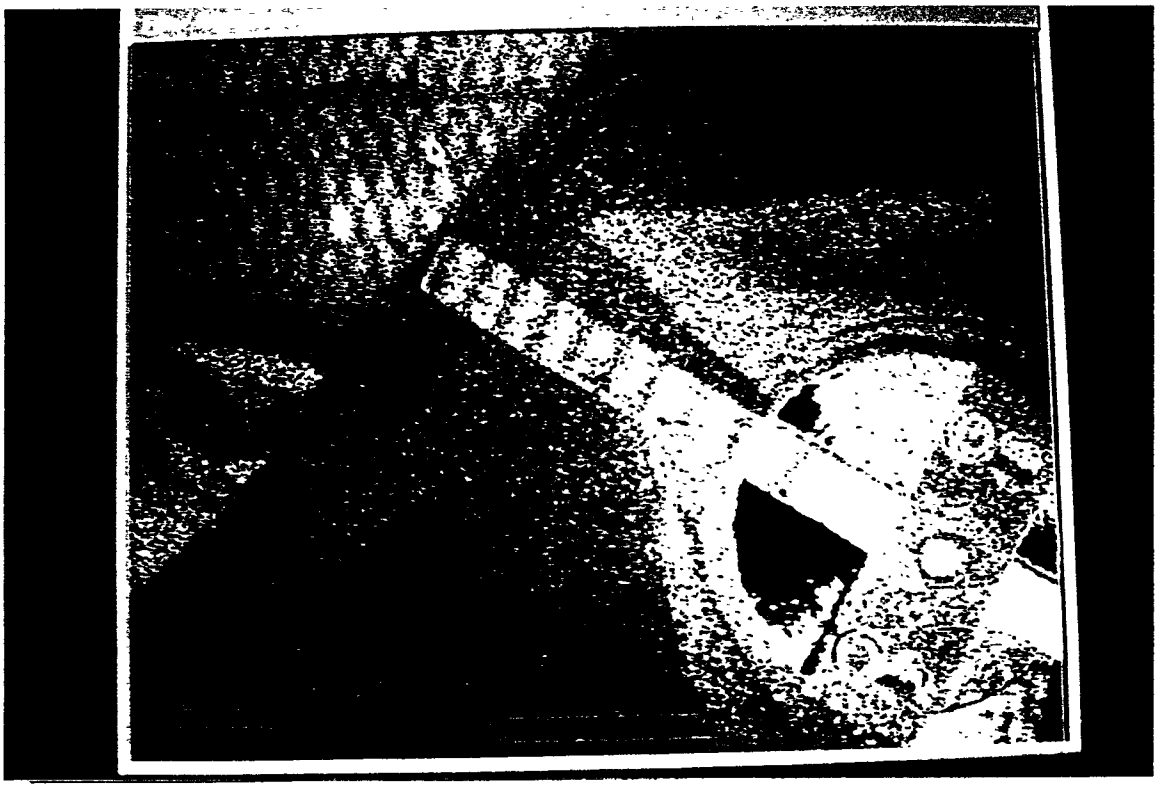

Figure 7 Typical resonance fringe pattern for a cantilevered sample.

Test Samples

In the preliminary tests we used, 1) a solid Al 5052 bar, 2) a solid Be-Cu bar, 3) an Al 5052 laminate, and 4) a Be-Cu laminate. The properties of the test samples are shown in **Table 1**. The Al laminate, provided by CSA Engineering, consisted of a viscoelastic core sandwiched between two .045 inch skins. We fabricated the Be-Cu laminate from a 5 mil viscoelastic core and two .025 inch skins.

Material	Thickness (in)	Width (in)	E_{theory} (psi)	ρ_{theory} (lb_m/in^3)
Al 5052	0.087	0.505	10.2E+06	2.51E-04
Be-Cu	0.055	0.982	18.5E+06	7.72E-04
Al laminate	0.101	0.515	?	?
Be-Cu laminate	0.058	1.013	?	?

Table 1 The material and dimensional properties of the test samples.

Preliminary Results

This is a report on the preliminary tests used to evaluate our experimental methods. They were not performed in a vacuum, and we did not incorporate an aerodynamic damping model for data reduction purposes, even though, from the literature [5], we know that aerodynamic damping effects can be significant for non-vacuum environments. As a result, the data and its interpretation are very preliminary. We believe these tests indicate the need for a better clamping support, because when the samples were clamped in the support, the resonance frequency changed with the passage of time, and the bending modulus decreased as the cantilevered length decreased. We also located two natural resonances of the shaker at 180 Hz and 990 Hz. Damping measurements near these frequencies are surely affected by these modes. We are presently attempting to improve our experimental setup so that damping measurements can be interpreted with greater confidence. Appendix I details the findings of all the preliminary tests. The section below presents a representative set of these results. The testing strains for these results range from .1 to 10 $\mu\varepsilon$.

Al 5052 and Be-Cu Samples

Loss factors for both the solid Al and solid Be-Cu samples are shown in **Table 2** and **Table 3**, respectively. The Al sample exhibits a consistently greater loss factor then the Be-Cu sample. The bending modulus (E) of both materials decrease as the resonance frequency increases.

Resonance Frequency (Hz)	Cantilevered Length (in)	Measured E (psi)	Loss Factor (η)
75.12	6.01	9.35E+06	2.53E-03
142.02	4.35	9.17E+06	2.11E-03
229.54	3.40	8.94E+06	1.74E-03
333.00	2.81	8.78E+06	1.98E-03
571.94	2.13	8.55E+06	1.64E-03

Table 2 Loss factors for the solid Al sample.

Resonance Frequency (Hz)	Cantilevered Length (in)	Measured E (psi)	Loss Factor (η)
76.63	3.88	13.0E+06	1.44E-03
149.19	2.76	12.6E+06	2.08E-03
240.05	2.15	12.1E+06	1.04E-03
337.14		*********	1.16E-03
574.54	1.34	10.4E+06	1.18E-03

Table 3 Loss factors for the solid Be-Cu sample.

Al and Be-Cu Laminate Samples

Table 4 shows the results from testing the Al laminate over a wide frequency range. The marked change in η with frequency seems to indicate that the material's response is frequency dependent. This could be accounted for if the skins vibrate together

at one frequency and vibrate out of phase with one another at a different frequency. The results for the Be-Cu laminate are depicted in **Table 5**. Since we only tested a small frequency range, no conclusions may be made about the material's frequency dependency.

Both laminates displayed symmetric resonance curves at specific frequencies, e.g. 1073 Hz and 125 Hz for the Al laminate. However, other resonance curves were complex and unsymmetric. We noticed what seemed to be a coupling of modes; a second mode mixing with the first. This behavior usually delayed the arrival of the half power point, and therefore increased the measured loss factor. These observations only strengthen the argument for experimental analysis of these laminate materials. It is doubtful that analytical or finite element models would have been able to characterize this response. These laminates also exhibited improved damping capacity, 100 times greater, as compared with their solid alloy counterparts.

Measured Frequencies (Hz)			Loss Factor
f_r	f_1	f_2	(η)
77.30	84.37	69.86	1.88E-01
104.11	124.74	91.79	3.16E-01
110.86	123.07	99.55	2.12E-01
128.46	141.13	113.36	2.16E-01
174.90	193.22	156.28	2.11E-01
232.17	243.97	213.10	1.33E-01
330.69	406.19	302.00	3.15E-01
530.38	610.25	477.28	2.51E-01
1,076.60	1,088.30	1,060.31	2.60E-02

Table 4 Loss Factors for Al laminate.

Measured Frequencies (Hz)			Loss Factor
f_r	f_1	f_2	(η)
76.25	84.88	68.03	2.21E-01
107.34	120.77	94.40	2.46E-01
120.57	137.01	105.47	2.62E-01
136.40	152.61	119.68	2.41E-01

Table 5 Loss Factors for Be-Cu laminate.

Future Work

In a few weeks of testing we were not been able to quantitatively understand the damping properties of the material samples we tested. These measurements are much more difficult than we first anticipated. Our first impression was, after all, what should be difficult about testing a cantilever beam? If we had known the literature beforehand, however, we would have anticipated many of the difficulties we encountered. At this point we believe our results indicate only the general range of material properties for the samples we tested. Considerably more testing is needed to understand the details. The preliminary tests point the way to improvements we can make in our experimental setup and methods so we can get better, more consistent results. We obviously need to change our clamp, be very careful with our clamping method and carefully prepare our test samples. We need a better method to excite the cantilever vibration, because we had to drive the damped beams so hard to start them vibrating that we excited modes in the shaker apparatus that affected the results. We should test the cantilevers in a vacuum to evaluate how air resistance affects the damping properties, and we should re-evaluate our testing method. TV holography is a very good method for observing the mode shape of parts during tests, but it is an awkward method to use to collect a lot of data. Since the resonance behavior we observed is far from linear, it is not sufficient to measure only a few points on a resonance curve to describe the material behavior. Many data points throughout the range of interest need to be collected. A method should be developed to scan the drive frequency and measure the vibration amplitude quickly. We are building a very sensitive fiber optic probe and LabView software that we believe would be ideal instrument for this measurement. We would like to use the probe to measure material properties at very low vibration amplitudes and strains. We would use TVH to determine the overall mode shape and use the fiber optic probe to collect many data points over a range of interest. We have all the equipment needed as well as a vacuum test tank to develop these ideas.

References

1. Macé, M., "Damping of Beam Vibrations by Means of a Thin Constrained Viscoelastic Layer: Evaluation of a New Theory", *J. of Sound and Vibration*, Vol. 172, No. 5, 1994, pp. 577-591.
2. Kerwin, E. M., "Damping of Flexural Waves by a Constrained Viscoelastic Layer", *J. of the Acoustical Society of America*, Vol. 31, No. 7, 1959, pp. 952-952.
3. Rao, D. K., "Frequency and Loss Factors of Sandwich Beams Under Various Boundary Conditions", *J. of Mechanical Engineering Science*, Vol. 20, No. 5, 1978, pp. 271-282.
4. Soni, M. L., "Finite Element Analysis of Viscoelastically Damped Sandwich Structures", *Shock and Vibration Bulletin*, Vol. 51, No. 1, May 1981, pp. 97-109.
5. Ting, J. M., Crawley, E. F., "Characterization of Damping of materials and Structures from Nanostrain Levels", NASA Space Engineering Center, Massachusetts Institue of Technology, SERC Rept. 1-90, June 1990.

Appendix I

Testing Aluminum Sample

We tested the Al sample at various frequencies, between 135 and 661 Hz, performing these tests rapidly with little concern given to the clamped boundary condition or the cantilevered length of the beam: only the resonance frequency and its associated half power points were recorded. The results from these tests exhibited a standard deviation of $\sigma_\eta = 5.86 \times 10^{-4}$ with a mean loss factor of $\eta = 3.4 \times 10^{-3}$.

As long as the pure beam bending model remains applicable, varying the cantilevered length should have no effect on Young's modulus (E). We used this result to help monitor our experimental accuracy. For the second set of tests, we marked the cantilevered length with a 0.5 mm pencil. The results, shown in **Table 6**, span the frequency range of 91-1143 Hz. For these tests, $\sigma_E = 5.41 \times 10^5$ with a mean value of E= 8.41×10^6, and $\sigma_\eta = 8.36 \times 10^{-4}$ with a mean loss factor of $\eta = 2.28 \times 10^{-3}$.

Measured Frequencies (Hz)			Measured	Young's	Loss Factor
f_r	f_1	f_2	Length (in)	Modulus (psi)	(η)
91.15	91.30	91.03	5.45	9.31E+06	2.96E-03
137.73	138.05	137.50	4.37	8.79E+06	3.99E-03
193.16	193.44	192.95	3.69	8.79E+06	2.54E-03
256.08	256.31	255.90	3.17	8.41E+06	1.60E-03
349.23	349.60	349.06	2.79	9.39E+06	1.55E-03
438.12	438.55	437.90	2.41	8.23E+06	1.48E-03
504.92	505.54	504.63	2.23	8.01E+06	1.80E-03
573.12	573.72	572.75	2.09	7.96E+06	1.69E-03
670.33	670.82	669.84	1.95	8.25E+06	1.46E-03
762.70	763.84	762.26	1.81	7.93E+06	2.07E-03
928.74	930.21	927.61	1.63	7.73E+06	2.80E-03
1,142.63	1,144.75	1,140.98	1.49	8.17E+06	3.30E-03

Table 6 Loss factors and measured Young's modulus for solid Al sample.

Due to the wide range in E, the support conditions of the beam, i.e. the clamp, were considered more closely. To provide a more consistent boundary condition, we

centered the clamp bolts in their slots and tightened them by hand with a screwdriver until the bolts could no longer be turned. Also, to improve the accuracy of the bending modulus calculations, we employed a razor blade to mark the beam next to the clamp. These tests reduced the standard deviation to $\sigma_E = 1.23 \times 10^5$ for a mean E of 9.27×10^6.

Testing Beryllium-Copper Sample

When testing began on the beryllium-copper sample, our attention again focused on the clamped boundary condition, and how it influenced the test data. We placed the Be-Cu sample into the clamp, marked its length with a razor blade and then tested it. We used a square to orient the sample at a right angle with respect to the clamp, and we started tightening the bolts with an Allen wrench, enabling larger torques to be applied. Additionally, we slid the clamp bolts forward in their slots, towards the base of the cantilever. After recording one set of data, we left the sample in the clamp and waited 5 to 10 minutes, and then we recorded more data. This was repeated several times with various intervals between tests. The results showed that over time, the resonance frequency of the sample steadily increased. Obviously something had changed, even though the sample, the clamp, and the support structure had remained undisturbed throughout the test. The total time between the first set of data and the last was about 85 minutes. In this time, the resonance frequency had risen 1.7 Hz.

This trend was repeatable and consistent for other similar tests. **Figure 8** shows that the resonance frequency rose 9.09 Hz in a 64 hour period. In most cases, the results show a decrease in the damping ratio with time. This is seen in **Figure 9** for the test which spanned 64 hours.

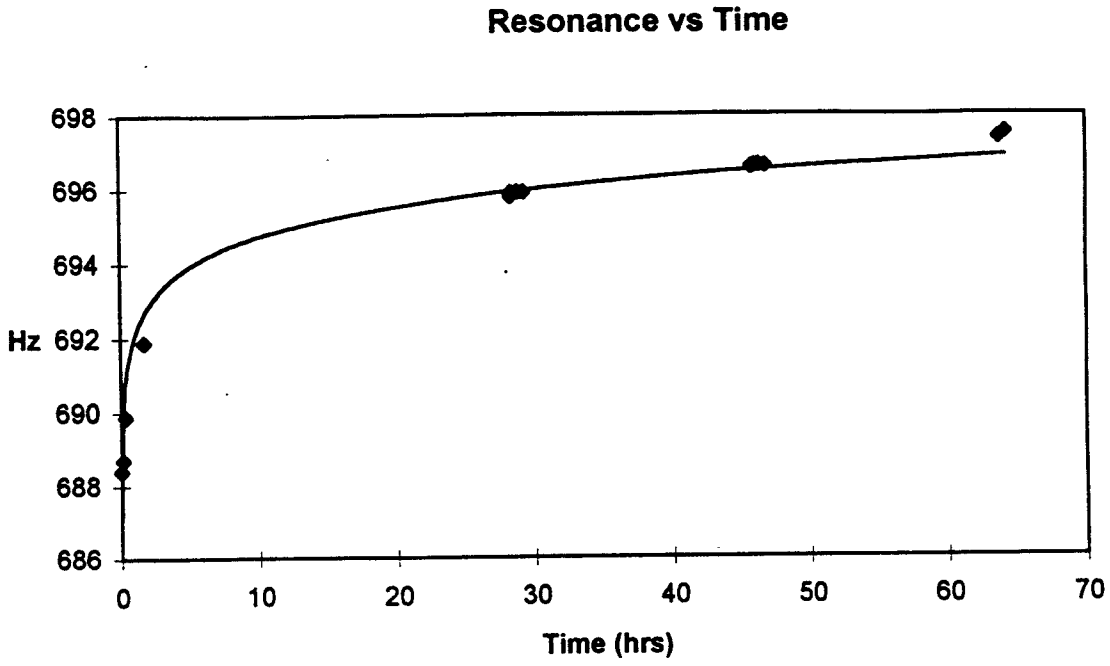

Figure 8 Plot showing how the resonance of a Be-Cu sample changes the longer it remains in the clamped support.

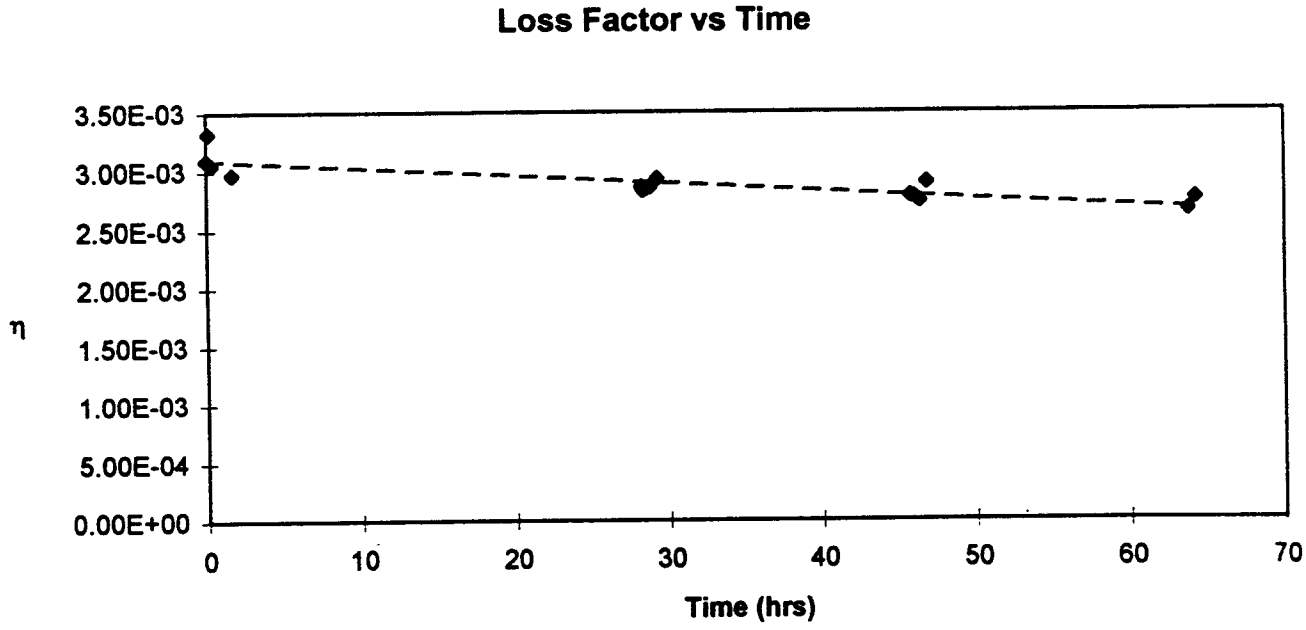

Figure 9 Plot showing how the loss factor of a Be-Cu sample decreases the longer it remains in the clamped support.

LIGO
Beam Tube Dynamic Analysis

April 28, 1994

T. Thompson **HYTEC, INC**

Preliminary Estimate of Beam Tube Motion Induced by Wind Noise

T. Thompson May 7, 1995

Background: Wind induced vibration of the beam tube enclosure is an extremely complicated phenomenon. This note will address a simplified approach for estimating the beam tube motion induced by wind noise. We view this as an opportunity to quantify the motion of the beam tube before one proceeds into a more elaborate and detailed prediction using a refined FEM.

The fluctuating forces and loads are due to the turbulence, vortex shedding and eddies. Under the extremely tight time constraints some simplifying assumptions were made in order to bound this problem. In the note from R.Weiss he gives some basis for estimating wind loading on structures similar to those proposed for LIGO. It is this author's understanding that the loading presented by Weiss is for an idealized half-cylinder in cross flow, not for an elliptical structure currently being shown by CBI. These equations were used to make some intelligent assumptions about what could be expected in the way of wind coupling into the LIGO enclosure and then into the beam tube itself.

Analysis: The analyses were performed to estimate the beam tube motion were more complicated than what was originally anticipated. Two finite element models ultimately were employed to get the frequency range desired by LIGO. The first finite element model, shown in Figure 1, consisted of shell, solid, and pipe elements to represent the elliptical beam tube enclosure, the concrete slab, the beam tube, and the soil surrounding the sides of the enclosure (10 meters deep by 15 meters wide). The beam tube enclosure will be fabricated from of an elliptical precast 5 inch concrete shell. The enclosure will sit on a concrete foundation which most likely will be 6 inches in thickness. For our model, the beam tube support was placed close to what is currently shown in the CBI plans, which shows the tube offset approximately 1 meter from the centerline of the enclosure. The second finite element model is a subset of the first and it has only the beam tube modeled (pipe elements), with a boundary condition simulating a rigid connection to the floor.

In the large finite element model the low frequency soil response tends to dominate the calculation of mode shapes. In this low frequency range, the modal extraction process generates a large number of modes solely associated with soil response. For this reason, it was impractical to use just one large model to obtain the beam tube response over the frequency range of interest.

For the foregoing reason, we chose to determine the beam tube response in two steps. The approach of using two models afforded an opportunity to determine coupled soil/slab/tube modes which could not be identified with the idealized tube used in the large model. This approximate analysis approach bounded many aspects of the problem, while providing valuable insight into this problem. It should be emphasized

that the primary objective was to "scope" the problem and determine the magnitude of vibration in the beam tube induced by wind loading.

Figure 2 shows the application of boundary conditions representing the wind load on the enclosure. This approximation to the wind loading as two discrete line loads, represent the drag and lift forces. This first order approximation cannot hope to capture the true pressure distribution on the structure which may ultimately be required in detailed simulation for LIGO.

The procedure used in this analysis was to use the equations developed by Weiss to estimate the input forcing function to the detailed model shown in Figure 1. This model because of it's large size captures only the first few beam tube modes. The dynamic results for this model quit at 25 Hz, which represent the first 75 modes of the model. The floor input vibration is captured from this model and transferred into the simpler beam tube model which has been used in prior analyses. This procedure should accurately capture most of the "interesting" vibratory modes. The slope, or roll-off, of the input vibrations decay rapidly with frequency in the larger model and this was also captured for input into the smaller model.

An assumption was made that the drag and lift force would be equal to one another for this effort. More detailed aerodynamic modeling could be undertaken later if needed in COSMOS to determine accurately the pressure loading around the enclosure. In addition, the point of application for the drag loads were placed approximately 1 meter off the floor, and at the apex of the enclosure for the lift loads. Although these locations are approximate, their placement will serve to quantify the displacement response of the structure.

The stop work order placed a time constraint on this task. It was not feasible to get all of the numeric results encompassing the lower wind speeds within the remaining time. We decided to present the "worst case" 50 MPH case. We presume the reader will scale the results to other wind velocities. This approach can be used since the "knee" in the critical frequency curve (f_c) fell well below our starting point of 2 Hz, for all wind speeds considered. The scaling factor is simply the ratio of the wind speeds raised to the 7/2 power. This factor is .0036 for 10 MPH and .021 for 30 MPH.

Results: The linearized displacement results for the beam tube are shown in Figures 3 through 5 for X, Y, and Z directions respectively. It is not apparent from figures, but in the large soil/slab/enclosure model there is a coupled mode at 12.1 Hz. We wish to point out that this coupling represents a factor of 4.5 increase in displacement over the previous "simple" beam tube model presented to LIGO through an earlier transmittal.

The results show that the anticipated maximum displacement of the beam tube is on the order of 25 microns at 12.1 Hz. It is our understanding that this magnitude will potentially pose a problem. The wind driven amplitude of the motions tend to roll off

quickly with frequency, hence above 30 Hz the ground noise will tend to be the dominant factor of motion in the beam tube.

Conclusions: The results of this analysis would tend to confirm that wind induced vibrations could be an issue. The beam tube does not sit on an optical floor which would tend to mitigate these forces. The beam tube sits on a relatively thin concrete slab which can be effectively coupled to the wind induced vibrations. Although, the wind induced vibration will roll off quickly, there may be some unacceptable vibrations below 30 Hz.

It may be appropriate to run more detailed solutions of this problems where more realism can be put into studying the affects of soil depth and breadth on their contribution to model results. We would recommend one study variants of design and how they affect the response. Topical examples are:

- enclosure and the slab structural joint
- pressure distribution (center of pressure) on the enclosure
- effect of the actual enclosure geometry on the anticipated coupling to the wind

One could argue that the occurrence of a 50 mph wind may be quite infrequent, and that from operational standpoint the experiment will simply stand down for a period of time. If this philosophy were not adopted, and the vibration of the beam tube remains an issue, some further study implementing clever isolation ideas may be appropriate.

References:

1. R. Weiss, *Preliminary Estimates for Wind Noise on the beam Tube Enclosure*, April 11, 1995

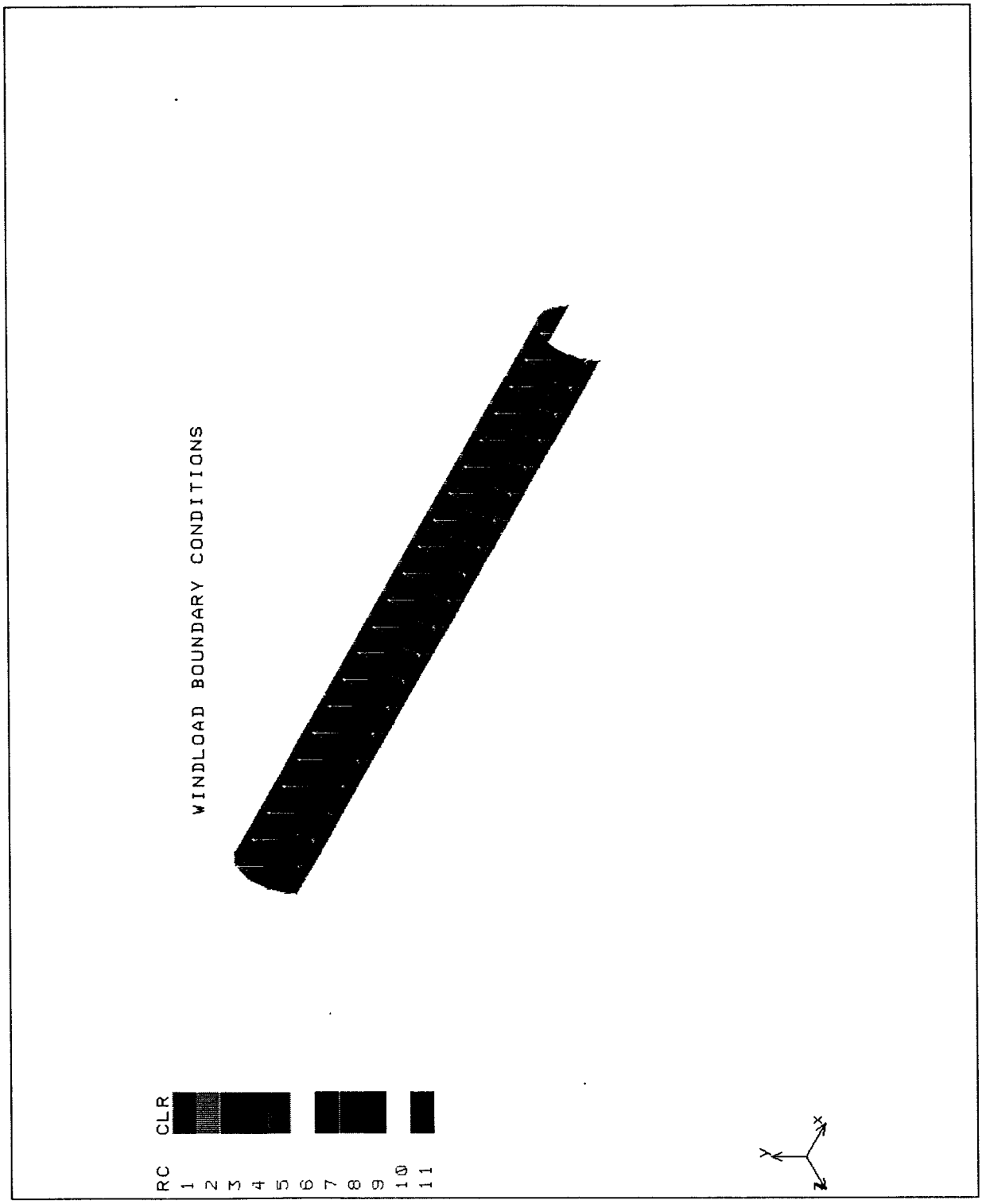

Figure 2. Wind Load Boundary Conditions on LIGO Enclosure.

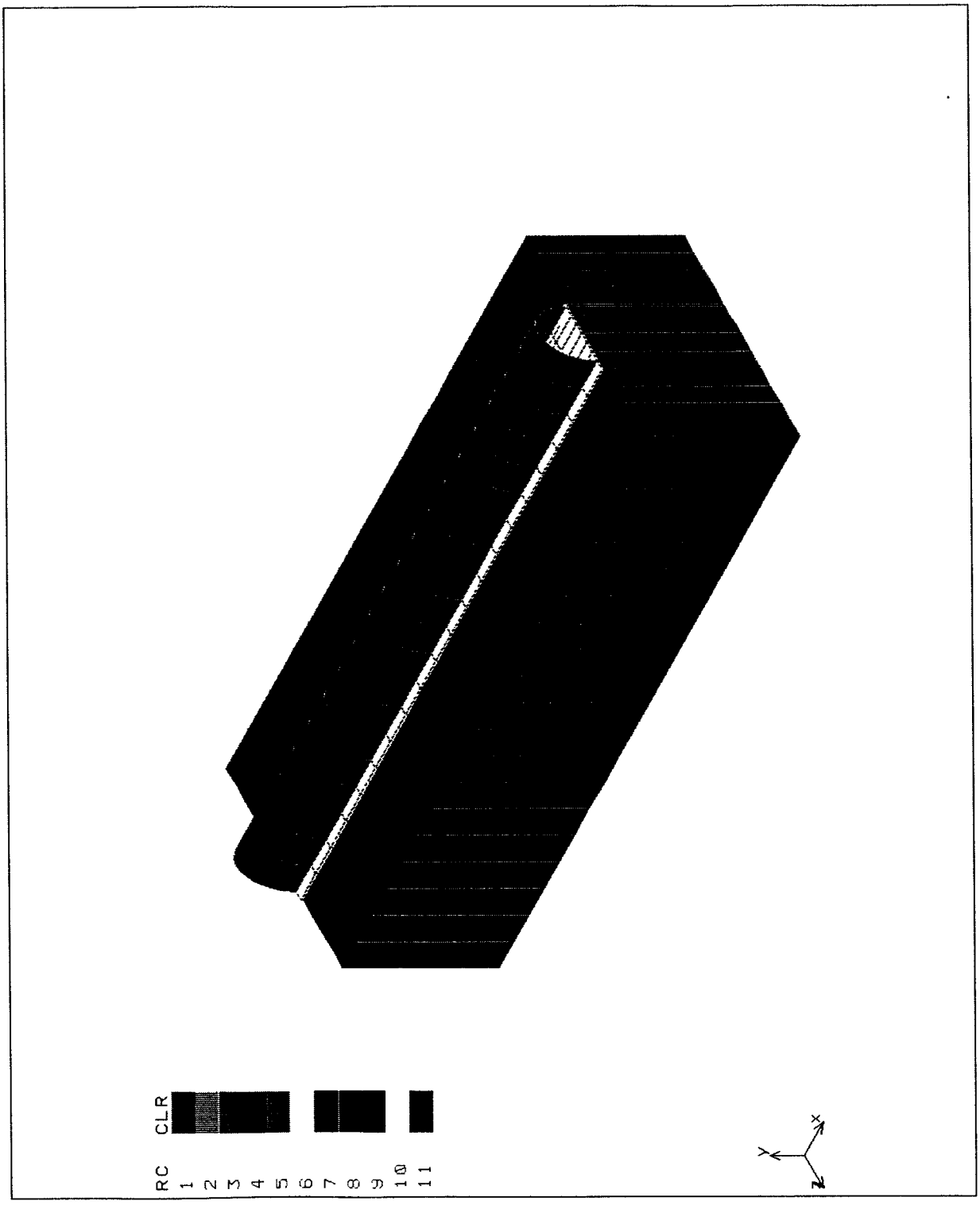

Figure 1. LIGO Soil/Slab/Enclosure and Beam Tube Finite Element Model.

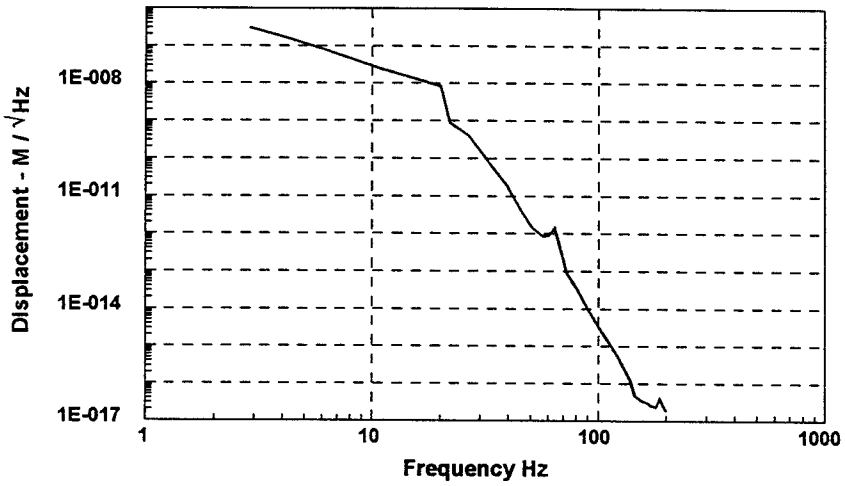

Figure 3. Linearized PSD, X-Direction showing small motions in the beamline direction

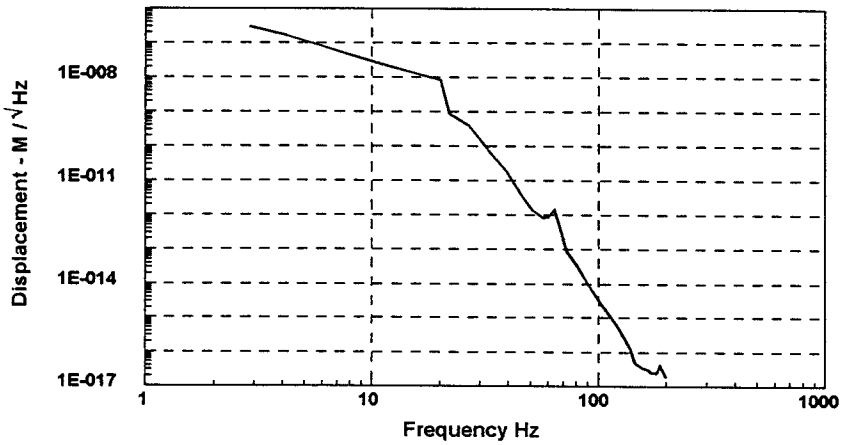

Figure 4. Linearized PSD, Y-Direction showing a peak resonance of 25 microns at 12.1 Hz

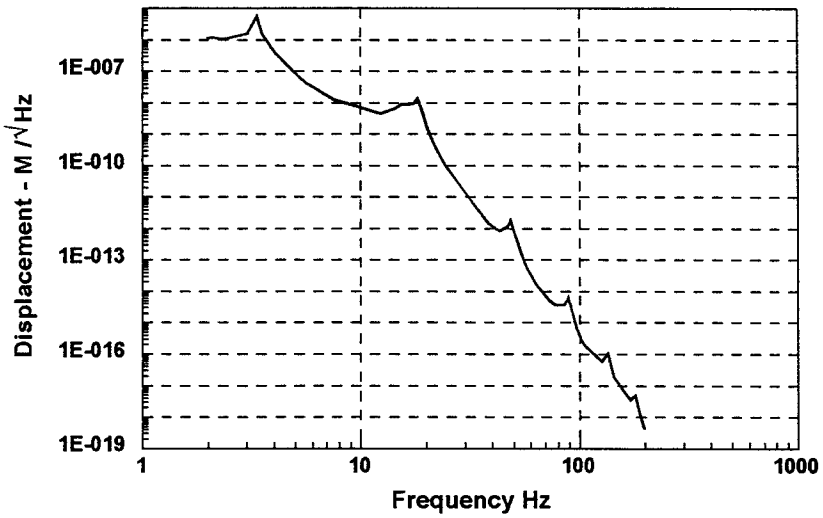

Figure 5. Linearized PSD Z-Direction with peak amplitudes of 25 microns at 3.9 Hz